A&A 675, A158 (2023)
https://doi.org/10.1051/0004-6361/202244611

Astronomy & Astrophysics

TOI-179: A young system with a transiting compact Neptune-mass planet and a low-mass companion in outer orbit⋆,⋆⋆

S. Desidera[1], M. Damasso[2], R. Gratton[1], S. Benatti[3], D. Nardiello[1,4], V. D'Orazi[1,5], A. F. Lanza[6], D. Locci[3], F. Marzari[7,1], D. Mesa[1], S. Messina[4], I. Pillitteri[3], A. Sozzetti[2], J. Girard[8], A. Maggio[3], G. Micela[3], L. Malavolta[9,1], V. Nascimbeni[1,9], M. Pinamonti[2], V. Squicciarini[1,9], J. Alcalá[10], K. Biazzo[11], A. Bohn[12], M. Bonavita[13,14,1], K. Brooks[15], G. Chauvin[16], E. Covino[10], P. Delorme[17], J. Hagelberg[18], M. Janson[19], A.-M. Lagrange[17], and C. Lazzoni[20,1]

[1] INAF – Osservatorio Astronomico di Padova, Vicolo dell'Osservatorio 5, 35122 Padova, Italy
e-mail: silvano.desidera@inaf.it
[2] INAF – Osservatorio Astrofisico di Torino, Via Osservatorio 20, 10025 Pino Torinese (TO), Italy
[3] INAF – Osservatorio Astronomico di Palermo, Piazza del Parlamento, 1, 90134 Palermo, Italy
[4] Aix-Marseille Univ., CNRS, CNES, LAM, 13000 Marseille, France
[5] Monash Centre for Astrophysics, School of Physics and Astronomy, Monash University, Clayton 3800, Melbourne, Australia
[6] INAF – Osservatorio Astrofisico di Catania, Via S. Sofia 78, 95123 Catania, Italy
[7] Dipartimento di Fisica e Astronomia – Universtà di Padova, Via Marzolo 8, 35121 Padova, Italy
[8] Space Telescope Science Institute, 3700 San Martin Drive, Baltimore, MD 21218, USA
[9] Dipartimento di Fisica e Astronomia – Universtà di Padova, Vicolo dell'Osservatorio 3, 35122 Padova, Italy
[10] INAF – Osservatorio Astronomico di Capodimonte, Salita Moiariello 16, 80131 Napoli, Italy
[11] INAF – Osservatorio Astronomico di Roma, Via Frascati 33, 00078 Monte Porzio Catone (Roma), Italy
[12] Leiden Observatory, Leiden University, PO Box 9513, 2300 RA Leiden, The Netherlands
[13] School of Physical Sciences, The Open University, Walton Hall, Milton Keynes MK7 6AA, UK
[14] SUPA, Institute for Astronomy, University of Edinburgh, Blackford Hill, Edinburgh EH9 3HJ, UK
[15] Laboratory for Atmospheric and Space Physics 1234 Innovation Dr. Boulder, CO 80303, USA
[16] Université Côte d'Azur, Observatoire de la Côte d'Azur, CNRS, Laboratoire Lagrange, Bd de l'Observatoire, CS 34229, 06304 Nice Cedex 4, France
[17] Univ. Grenoble Alpes, CNRS, IPAG, 38000 Grenoble, France
[18] Observatoire de Genève, Université de Genève, 51 Ch. des Maillettes, 1290 Sauverny, Switzerland
[19] Department of Astronomy, Stockholm University, 106 91 Stockholm, Sweden
[20] University of Exeter, Astrophysics Group, Physics Building, Stocker Road, Exeter EX4 4QL, UK

Received 27 July 2022 / Accepted 25 September 2022

ABSTRACT

Context. Transiting planets around young stars are key benchmarks for our understanding of planetary systems. One such candidate, TOI-179, was identified around the K dwarf HD 18599 by TESS.
Aims. We present the confirmation of the transiting planet and the characterization of the host star and of the TOI-179 system over a broad range of angular separations.
Methods. We exploited the TESS photometric time series, intensive radial velocity monitoring performed with HARPS, and deep high-contrast imaging observations obtained with SPHERE and NACO at VLT. The inclusion of Gaussian process regression analysis was effective to properly model the magnetic activity of the star and identify the Keplerian signature of the transiting planet.
Results. The star, with an age of 400±100 Myr, is orbited by a transiting planet with period 4.137436 days, mass 24±7 $M_\oplus$, radius $2.62^{+0.15}_{-0.12}\,R_\oplus$, and significant eccentricity ($0.34^{+0.07}_{-0.09}$). Adaptive optics observations identified a low-mass companion at the boundary between brown dwarfs and very low-mass stars (mass derived from luminosity $83^{+4}_{-6}\,M_J$) at a very small projected separation (84.5 mas, 3.3 au at the distance of the star). Coupling the imaging detection with the long-term radial velocity trend and the astrometric signature, we constrained the orbit of the low-mass companion, identifying two families of possible orbital solutions.
Conclusions. The TOI-179 system represents a high-merit laboratory for our understanding of the physical evolution of planets and other low-mass objects and of how the planet properties are influenced by dynamical effects and interactions with the parent star.

Key words. planetary systems – stars: individual: HD 18599 – planets and satellites: individual: TOI-179b – binaries: close – techniques: radial velocities – techniques: high angular resolution

⋆ Based on observations made with ESO Telescopes at the La Silla Paranal Observatory under program IDs 192.C-0224(C), 098.C-0739(A), 0101.C-0510(D), 0102.C-0451(B), 0102.D-0483(A), 0102.C-0525(A) 0103.C-0759(A) (HARPS), 0104.C-0247(B) (SPHERE), 097.C-0972(A) (NACO).
⋆⋆ This paper includes data collected by the TESS mission, which are publicly available from the Mikulski Archive for Space Telescopes (MAST).

1. Introduction

The observed architecture of a planetary system takes shape after significant evolution of the system itself has occurred over time, with several mechanisms acting on different timescales: migration within the native disk (Lin et al. 1996), expected to occur a few million years before disk dissipation; planet-planet dynamical instabilities (Weidenschilling & Marzari 1996); gravitational interactions with passing bodies (more frequent for stars in clusters, Bonnell et al. 2001) and bound companions on wide orbits (e.g., through the Kozai mechanisms; Wu et al. 2007), and circularization of the orbit by tides from the host stars (Rasio et al. 1996), which could be active on much longer timescales. Understanding the original configurations of the systems and the timescales on which these various mechanisms work is easier when observing planetary systems at young ages, with planets closer to their formation time epoch and possibly also to their birthsites. Young ages also offer the unique opportunity of accessing the range of wide separations through direct imaging with sensitivity into the planetary regime, as young planets are brighter (Chauvin 2018). Furthermore, the outer planets in planet-planet scattering events are expected to be lost with time and then more easily identified close to the parent stars at young ages (Veras et al. 2009). A large number of companions at wide separations was identified for some classes of planetary systems (e.g., Bryan et al. 2019; Fontanive et al. 2019).

Transit space missions are deeply changing our view of planetary systems at close separations. A large fraction of (old) G, K, and M stars were found to host low-mass planets (e.g., Howard et al. 2012; Bryson et al. 2021). These planets show a large variety of system architectures and internal structures, as inferred by bulk density measurements. However, most targets of the first missions CoRoT and Kepler are very distant (≥0.5 kpc). The large distance and faintness make them prohibitive targets for direct imaging characterization, limiting searches to wide stellar companions (e.g., Horch et al. 2014; Hirsch et al. 2017). The large distances, the confined observations to well-defined fields, and the faint magnitude of the stars also represent major challenges for a proper age estimation of these targets, exploiting spectroscopic diagnostics, isochrone fitting, or kinematics. Instead, the Transiting Exoplanet Survey Satellite (TESS) mission (Ricker et al. 2015) offers a much better perspective as it covers nearly the whole sky and targets closer and brighter objects than those observed with Kepler. Therefore, nearby young stars with well-characterized ages, members of moving groups, star clusters, and even isolated field stars are being searched for planetary transits. Previously, Kepler/K2 also monitored several fields centered on star forming regions and young clusters (Rizzuto et al. 2017).

Transiting planets at young ages are key benchmarks for our understanding of planetary systems. There are several reasons for this. First, their frequency at various ages allows us to constrain the timescales of the migration mechanisms. Second, their radii are expected to be expanded with respect to those of older planets of similar masses (Linder et al. 2019). Third, their expected low density and large scale heights make them prime targets for atmospheric characterization. Planetary evaporation processes are expected to be stronger in these cases where the planets are close enough to their parent stars. In addition, for late-type host stars, the impact of very high levels of stellar magnetic activity on the planetary atmospheres can be studied. Fourth, for giant planets, their structure and atmospheric properties can be compared to those of non-irradiated planets of similar ages at wide separation, detected and characterized with the imaging technique. Finally, the transit geometry itself and the Rossiter–McLaughlin effect provide additional constraints on the architecture of the system, not available for planets detected only with the radial velocity (RV) technique.

Promising results have emerged from several efforts over the past few years. These include the discovery of young multiplanet systems such as V1298 Tau (David et al. 2019) and AU Mic (Plavchan et al. 2020), with determination of the masses of some planets in these systems obtained through intensive RV monitoring campaigns (Suárez Mascareño et al. 2021; Klein et al. 2021; Zicher et al. 2022). Several other young transiting planets were identified around stars which are members of open clusters (e.g., Bouma et al. 2020), stellar associations and moving groups (e.g., Rizzuto et al. 2020; Newton et al. 2021), or field objects (e.g., Zhou et al. 2021; Barragán et al. 2022); in many cases these planets still lack reliable mass determinations as the observational efforts to overcome the noise linked to stellar activity are great for such active stars. Additional characterization studies were performed in a few cases, such as the measurement of the Rossiter–McLaughlin effect (e.g., Mann et al. 2020).

Our team started to work on TESS datasets with the first sector of TESS observations, which included a planet candidate around DS Tuc, a bona fide member of the Tuc-Hor association (age 40–45 Myr). The transiting planet candidate detected by TESS was validated independently by Benatti et al. (2019) and Newton et al. (2019) and further characterized by Benatti et al. (2021). Northern young targets are being followed up in the framework of the GAPS program (Carleo et al. 2020), starting from the validation of the two-planet system around TOI-942, a 50 Myr old K star (Carleo et al. 2021), and the measurement of the mass of the ultra-short-period planet TOI-1807b around a 300 Myr old star (Nardiello et al. 2022).

As part of ongoing efforts to validate and characterize young transiting exoplanets identified by TESS, in this paper we present our analysis for the system observed around the star HD 18599 = HIP 13754, a bright (V = 8.99 mag) and active K dwarf, also known as TESS Object of Interest 179 (TOI-179). The planet candidate was identified from TESS observations gathered in Sectors 2–3. The star was also observed by TESS during Sectors 29–30. It is a single-planet candidate with a radius of 2.6 $R_\oplus$ and a period of 4.1375 days, according to the TOI release information[1]. It was the target of our dedicated investigations using HARPS RV monitoring and high-contrast imaging observations with SPHERE and NaCo.

The paper is organized as follows. Section 2 presents the photometric, spectroscopic, and high-contrast imaging observations. Section 3 summarizes the stellar parameters (whose determination is described in detail in Appendix A). Section 4 presents the confirmation and mass determination of the transiting planet TOI-179b. Section 5 reports the detection of a low-mass companion at the brown dwarf (BD)–star boundary. In Sect. 6, we discuss the various implications of our findings, and in Sect. 7 we summarize our results and the perspectives for further characterization.

2. Observations and data reduction

2.1. Photometric observations with TESS

In this work, we made use of TESS long-cadence (30- and 10-min) and short-cadence (2-min) observations. Long-cadence data were used to perform a series of vetting tests and to confirm the planetary nature of TOI-179 b (Sect. 4.1), and to measure

[1] https://tess.mit.edu/toi-releases/

the rotation period (Appendix A.6), while short-cadence observations were adopted to model the planetary transits (Sect. 4.3).

2.1.1. Long-cadence light curves from Full Frame Images

We used the Full Frame Images (FFIs) collected by TESS during Cycles 1 and 3 to extract the light curves of TOI-179. This object was observed in 2018, between August 22 and October 18 in 30-min cadence mode (Sectors 2 and 3), and again in 2020, between August 26 and October 21 in 10-min cadence mode (Sectors 29 and 30). For the extraction of the light curves we used the light curve extractor developed by Nardiello et al. (2015, 2016) and adapted to TESS data by Nardiello et al. (2019). Briefly, given a target star, the software subtracts from the FFIs all its neighbors by using information from an input catalog (*Gaia* DR2) and empirical point spread functions (PSFs). After the subtraction, it extracts the flux of the target star by using five different photometric apertures. The systematic effects that affect the light curves are finally corrected by fitting to them the cotrending basis vectors extracted as described in Nardiello et al. (2020).

2.1.2. Short-cadence light curves

TOI-179 was observed by TESS in 2-min cadence mode in Sectors 2, 3, 29, and 30 via target pixel stamp observations, and it was included in the following TESS Guest Investigator Programs: GO3102 (PI: T. Oswalt), GO3227 (PI: J. Davenport), GO3272 (PI: J. Burt), and GO3278 (PI: A. Mayo). In this work we used the Pre-search Data Conditioning Simple Aperture Photometry (PDCSAP) light curves (Smith et al. 2012; Stumpe et al. 2012, 2014) from the Science Processing Observation Center (SPOC, Jenkins et al. 2016), which were extracted from the 2-min target pixel files.

2.2. Spectroscopic observations with HARPS

We obtained high-resolution spectra of TOI-179 within a dedicated follow-up program with HARPS (Mayor et al. 2003) at the ESO 3.6 m telescope (La Silla Observatory, Chile, Program ID 0103.C-0759(A), PI Benatti). From July 6 to September 22, 2019, we collected 40 spectra of TOI-179 with a typical exposure time of 900 s and a signal-to-noise ratio (S/N) of about 60. Additional spectra were collected under different ESO programs (192.C-0224 and 098.C-0739, PI Lagrange; 0101.C-0510, PI Jordan; 0102.C-0451 PI Brahm; 0102.D-0483, PI Berdinas; and 0102.C-0525, PI Diaz) and retrieved from the ESO archive. Part of the early dataset was published independently by Grandjean et al. (2020), with the RVs derived through the SAFIR software. Overall, in this work we analysed 103 radial velocity measurements of TOI-179, with a time baseline of 1768 d (from November 19, 2014, to September 22, 2019).

We measured the RVs by using the Template Enhanced Radial velocity Reanalysis Application (TERRA) pipeline (v1.8; Anglada-Escudé & Butler 2012), which is more effective and less affected by stellar activity features of young and active stars than the method based on the cross-correlation function (CCF; Damasso et al. 2020). TERRA allowed us to obtain a uniform set of reductions of all the spectra obtained from different observational campaigns. Seven spectra were collected before the fiber upgrade intervention on the HARPS spectrograph occurred in May 2015, which introduced an average RV offset of $\sim$16 m s^{-1} for G-type slowly rotating stars, as reported by Lo Curto et al. (2015). We treated these seven spectra (HARPS-pre) and the remaining 96 spectra (HARPS-post) as datasets coming from different instruments, both when extracting the RVs (which includes an additional offset) and when modeling the time series. The typical values (median) of the RV errors is 1.4 m s^{-1}. Figure 1 (upper panel) shows the RVs for TOI-179 superimposed by a simple linear fit that we used to remove the trend (lower panel) to evaluate the RV dispersion (24.5 m s^{-1}), which is likely dominated by the contribution of the stellar activity. For better visualization, we applied an RV offset to the HARPS-pre spectra by using the coefficients of the linear trend.

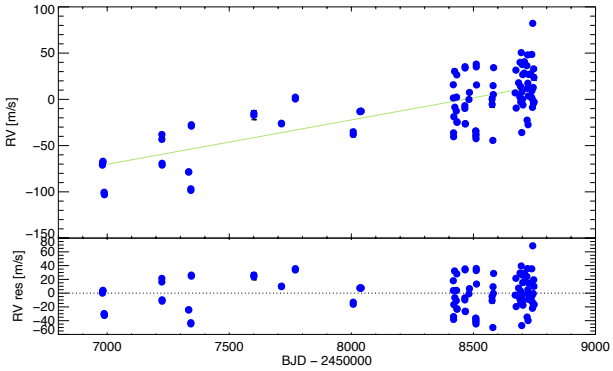

Fig. 1. HARPS RV time series of TOI-179. The green line in the upper panel depicts a linear interpolation of the long-term trend. The lower panel shows the residuals of the model.

We also considered the data products of the instrument pipeline[2] to evaluate the bisector velocity span (BIS) and the FWHM of the CCF. Finally, we also exploited the HARPS spectra to measure activity indices and to derive the stellar properties (see Sect. 3, and Appendices A.1–A.6). The time series are listed in Appendix B.

2.3. High-contrast imaging

2.3.1. SPHERE

We observed TOI-179 with the VLT high-contrast imaging instrument SPHERE (Beuzit et al. 2019) during the nights of 2019 October 11 and 2019 December 18, under the open time program 0104.C-0247(B), (P.I. S. Desidera). The first observation was acquired using the IRDIFS observing mode with IFS (Claudi et al. 2008) operating in the Y and J spectral bands (between 0.95 and 1.35 μm) and with IRDIS (Dohlen et al. 2008) operating in the H spectral band with the $H23$ filter pair (wavelength $H2$ = 1.593 μm; wavelength $H3$=1.667 μm; Vigan et al. 2010). The second observation was performed exploiting the IRDIFS_EXT observing mode with IFS operating in the Y, J, and H spectral bands (between 0.95 and 1.65 μm) and with IRDIS operating in the K spectral band using the $K12$ filter pair (wavelength $K1$=2.110 μm; wavelength $K2$ = 2.251 μm). The main characteristics of the two observations are listed in Table 1. In both cases, a 3072 s long sequence of coronagraphic images in pupil stabilized mode was performed, including meridian passage to optimize the speckle subtraction through angular differential imaging techniques. Furthermore, short non-coronagraphic images were taken before and after the coronagraphic sequence, to serve as PSF reference to calibrate the contrast curve and to explore the inner $\sim$0.12″ for bright companions.

[2] https://www.eso.org/sci/facilities/lasilla/instruments/harps/tools/archive.html

Table 1. Main characteristics of the AO observations of TOI-179 used for this work.

Date	Instr.	Obs. mode	Coronograph	DIMM seeing	τ_0	Wind speed	Field rot.	DIT	Total exp.
2016 Aug. 10	NaCo	L'	None	1.55	1.9 ms	12.48	16.3°	0.2 s	888.8 s
2019 Oct. 11	SPHERE	IRDIFS	N_ALC_YJH_S	1.18″	2.8 ms	9.53 m s^{-1}	22.0°	96 s	3072 s
2019 Dec. 18	SPHERE	IRDIFS_EXT	N_ALC_YJH_S	0.75″	5.2 ms	9.32 m s^{-1}	22.4°	96 s	3072 s

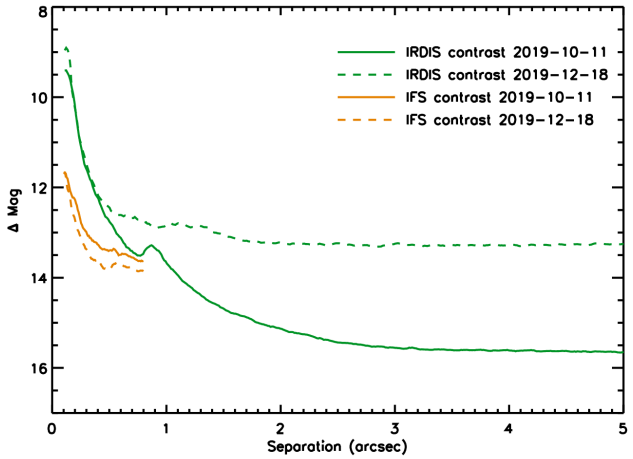

Fig. 2. Contrast plot in ΔMag for TOI-179 for both the SPHERE observing epochs. Green lines are for the IRDIS contrast, orange lines for the IFS contrast. Solid lines are for the 2019 October 11 epoch, dashed lines for the 2019 December 18 epoch.

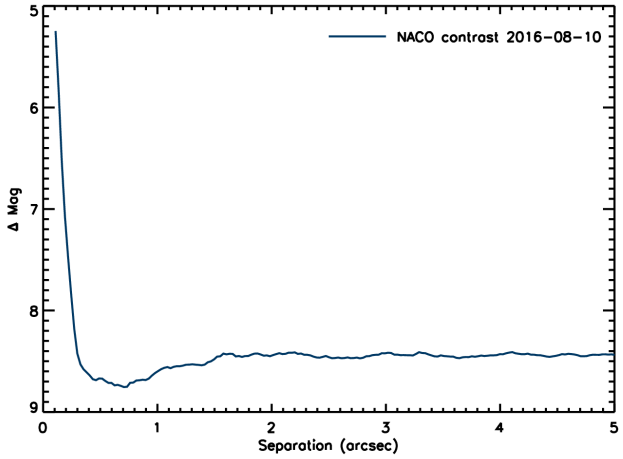

Fig. 3. Contrast plot in ΔMag for TOI-179 obtained using the NACO data.

We reduced the data through the SPHERE data center (Delorme et al. 2017) applying the appropriate calibrations following the data reduction and handling (DRH; Pavlov et al. 2008) pipeline. In the IRDIS case, the requested calibrations are the dark and flat-field correction and the definition of the star center. IFS requires, in addition to the dark and flat-field corrections, the definition of the position of each spectrum on the detector, the wavelength calibration, and the application of the instrumental flat. On the pre-reduced data we then applied speckle subtraction algorithms, for example Template Locally Optimized Combination of Images (TLOCI; Marois et al. 2014) abbreviation to introduce? see note 3 and principal components analysis (PCA; Soummer et al. 2012) as implemented in the SPHERE consortium pipeline application called SpeCal (Galicher et al. 2018), and also described in Zurlo et al. (2014) and in Mesa et al. (2015) for the IFS case.

We defined the contrast around the central star for both instruments and for both epochs exploiting the procedure described in Mesa et al. (2015) and corrected for the small sample statistic following the method described by Mawet et al. (2014). The final results of this procedure are displayed in Fig. 2.

The non-coronagraphic images obtained with IFS were analyzed using the custom procedure described in Engler et al. (2020); Bonavita et al. (2022b). This procedure subtracts the static aberrations in the PSF by comparing the non-coronagraphic images obtained before and after the coronagraphic images, exploiting the field rotation between them. A S/N map is then generated using channels at different wavelengths, and position of peaks with $S/N > 8$ are then checked. Candidates are kept only if this position is found to be independent of wavelength, since the position corresponding to bright speckles are expected to be wavelength dependent.

2.3.2. NaCo

The star was observed with NaCo on 2016 August 10 (see Table 1) in the context of the open time program 097.C-0972(A) (P.I. J. Girard). The observation was performed in L' band without coronograph and in pupil stabilized mode with a total rotation of the field of view (FoV) of 16.3°. The dataset was composed of 44 data cubes, each with 101 frames. The exposure time for each frame was 0.2 s for a total observing time of 888.8 s (less than 15 min). The star PSF was in different positions across the detector during the observations allowing us to effectively handle the bad pixels.

We created a master flat by making a median on the whole dataset, and we subtracted the resulting image from each frame of the raw data. We then performed a simple angular differential imaging (ADI) procedure on the reduced dataset to make the stellar noise lower.

The procedure to infer contrast limits was also exploited on the NaCo data. The results are displayed in Fig. 3.

2.4. Chandra observations

Chandra observed TOI-179 in two visits (OBsID 13481 and 14448, at epochs 2012 Jun 23 and 2012 Jun 24, respectively) for 22 and 26 ks, respectively. We downloaded the latest calibrated datasets and event lists and extracted the spectra and light curves of TOI-179 and its wide companion CD-56 583 (see Appendix A.8) with CIAO 4.14 and *dmextract*. We defined two circular regions with a radius of about 25″ to extract the events related to each source and background. For CD-56 583 the source extraction region includes both components. The task *dmextract* accumulates the spectra of source and background, calculates the response files, and groups the spectra to a minimum of 20 counts per bin so that they are suitable for the best-fit analysis. We used XSPEC v12.11.1b to analyze the grouped

spectra, within which we defined a model of coronal emission composed by a thermal optically thin plasma (APEC) absorbed by a global equivalent H column (TBAbs). We set a fixed low-absorption N_H value of 10^{17} cm^{-2} and metal abundance pattern ($Z = 0.2\ Z_\odot$) and left kT and spectrum normalization free to vary. The spectra from the two observations were fitted simultaneously. These data are used in Appendices A.5 and A.8 to infer the X-ray luminosity of the components of the system.

3. Summary of stellar parameters

TOI-179 has been recognized as an active star (Jenkins et al. 2008, 2011), but to date with a limited number of studies in the literature. It was included in the RV search for planets around young stars carried out by Grandjean et al. (2020). It was also in the sample of the SPHERE SHINE GTO survey as a low-priority target (Desidera et al. 2021), but was left unobserved at the end of the survey.

We performed our own determination of stellar parameters, exploiting the HARPS spectra, the TESS photometric time series, and the *Chandra* observations described in Sect. 2, coupled with additional data and results from the literature. These determinations are discussed in detail in Appendix A and the adopted parameters are summarized in Table 2.

In brief, the age indicators of TOI-179 consistently support an age older than the Pleiades and younger than the Hyades. After comparison with the 300 Myr old Group X association (Messina et al. 2022) we infer an age of 400 Myr with limits between 300 and 500 Myr. The star is an early K dwarf (Appendix A.1) with roughly solar chemical composition, according to the analysis of several elements performed in Appendix A.2. The stellar mass and radius are 0.863±0.020 $M_\odot$ and 0.767±0.024 $R_\odot$, respectively. An edge-on orientation is derived for the star from the observed rotation period, projected rotation velocity, and stellar radius, suggesting alignment with respect to the orbit of the transiting planet TOI-179b. Finally, TOI-179 forms a triple system with the close pair of late K dwarfs CD-56 593A and B (relative separation ∼1″), at a projected separation of 87.5″ from TOI-179 corresponding to 3400 au at the distance of the system (38 pc), as described in Appendix A.8. The physical association is confirmed by *Gaia* astrometry. The system is not a member of a group or association, as found in the analysis performed in Appendix A.7.

Table 2. Stellar properties of TOI-179.

Parameter	TOI-179	Ref
α (J2000)	02 57 02.95	*Gaia* EDR3
δ (J2000)	–56 11 31.51	*Gaia* EDR3
μ_α (mas/yr)	–36.661±0.015	*Gaia* EDR3
μ_δ (mas/yr)	50.558±0.015	*Gaia* EDR3
RV (km s^{-1})	–0.48±0.26	*Gaia* DR2
RV (km s^{-1})	–0.20±1.70	Jenkins et al. (2011)
π (mas)	25.8847±0.0128	*Gaia* EDR3
U (km s^{-1})	–3.562±0.011	Gaia Collaboration et al. (2021)
V (km s^{-1})	8.924±0.151	Gaia Collaboration et al. (2021)
W (km s^{-1})	–.223±0.203	Gaia Collaboration et al. (2021)
V (mag)	8.99	HIPPARCOS
$B-V$ (mag)	0.876±0.005	HIPPARCOS
$V-I$ (mag)	0.92±0.01	HIPPARCOS
G (mag)	8.7312±0.0007	*Gaia* DR2
BP–RP (mag)	1.073	*Gaia* DR2
J_{2MASS} (mag)	7.428±0.018	2MASS
H_{2MASS} (mag)	7.029±0.015	2MASS
K_{2MASS} (mag)	6.883±0.020	2MASS
T (mag)	8.180±0.006	TIC
Spectral type	K2V	Gray et al. (2006)
T_{eff} (K)	5172±60	This paper (spec) (Appendix A.1)
T_{eff} (K)	5118±60	This paper (phot) (Appendix A.1)
T_{eff} (K)	5145±50	This paper (adop.) (Appendix A.1)
log g	4.54±0.09	This paper (Appendix A.1)
[Fe/H] (dex)	0.00±0.08	This paper (Appendix A.1)
S_{MW}	$0.606^{+0.067}_{-0.086}$	This paper (Appendix A.5)
log R'_{HK}	$-4.35^{+0.05}_{-0.08}$	This paper (Appendix A.5)
$v \sin i$ (km s^{-1})	4.5±0.5	This paper (Appendix A.4)
P_{rot} (d)	8.73±0.07	This paper (Appendix A.6)
log L_X	28.51	This paper (Appendix A.5)
log L_X/L_{bol}	–4.65	This paper (Appendix A.5)
EW_{Li} (mÅ)	39.3±4.5	This paper (Appendix A.3)
A(Li)	1.55±0.08	This paper (Appebdix A.3)
Mass ($M_\odot$)	0.863±0.020	This paper (Appendix A.10)
Radius ($R_\odot$)	0.767±0.024	This paper (Appendix A.10)
Luminosity ($L_\odot$)	0.372±0.012	This paper (Appendix A.10)
Age (Myr)	400±100	This paper (Appendix A.9)

4. Confirmation of a low-mass transiting planet around TOI-179

4.1. TESS light curve analysis

The candidate exoplanet TOI-179b was detected for the first time by the Quick-Look Pipeline (QLP, Huang et al. 2020) using data from Sectors 2 and 3. We used the light curves extracted from the FFIs described in Sect. 2.1 to perform a series of vetting tests based on the TESS data to confirm this candidate exoplanet. A complete description of these tests is reported in Nardiello (2020). First, we modeled and removed the variability of the star from the light curve by interpolating it with a fifth-order spline defined on a series of knots spaced 6.5 h apart. During this procedure, we also removed all the points with the photometric flag `DQUALITY>0`. We detected the transit signals of the candidate exoplanets by extracting the transit least-squares (TLS) periodogram (Hippke & Heller 2019) of the flattened light curve, searching for transits between 0.5 days and 150.0 days. In this way we confirmed the periodic transit signal at $P \sim 4.1374$ days reported by the QLP report. An overview of the transit times for TOI-179b is reported in panel a of Fig. 4. The same figure shows that odd and even transits have the same depth within the errors (panel b) and that there is no correlation between the transit events and the X and Y-position of the star calculated by fitting to it the PSF in each image (panel c). Even if the star is isolated, we performed the analysis of in- and out-of transit difference centroid (panel d): within the errors ($<3\sigma$), the mean centroid calculated for each sector coincides with the position of the star.

4.2. Frequency content analysis of the radial velocities

Before performing a more complex analysis, we investigated the frequency content in the RV time series by calculating the generalized Lomb–Scargle (GLS, Zechmeister et al. 2009) periodogram. We were particularly interested in inspecting the

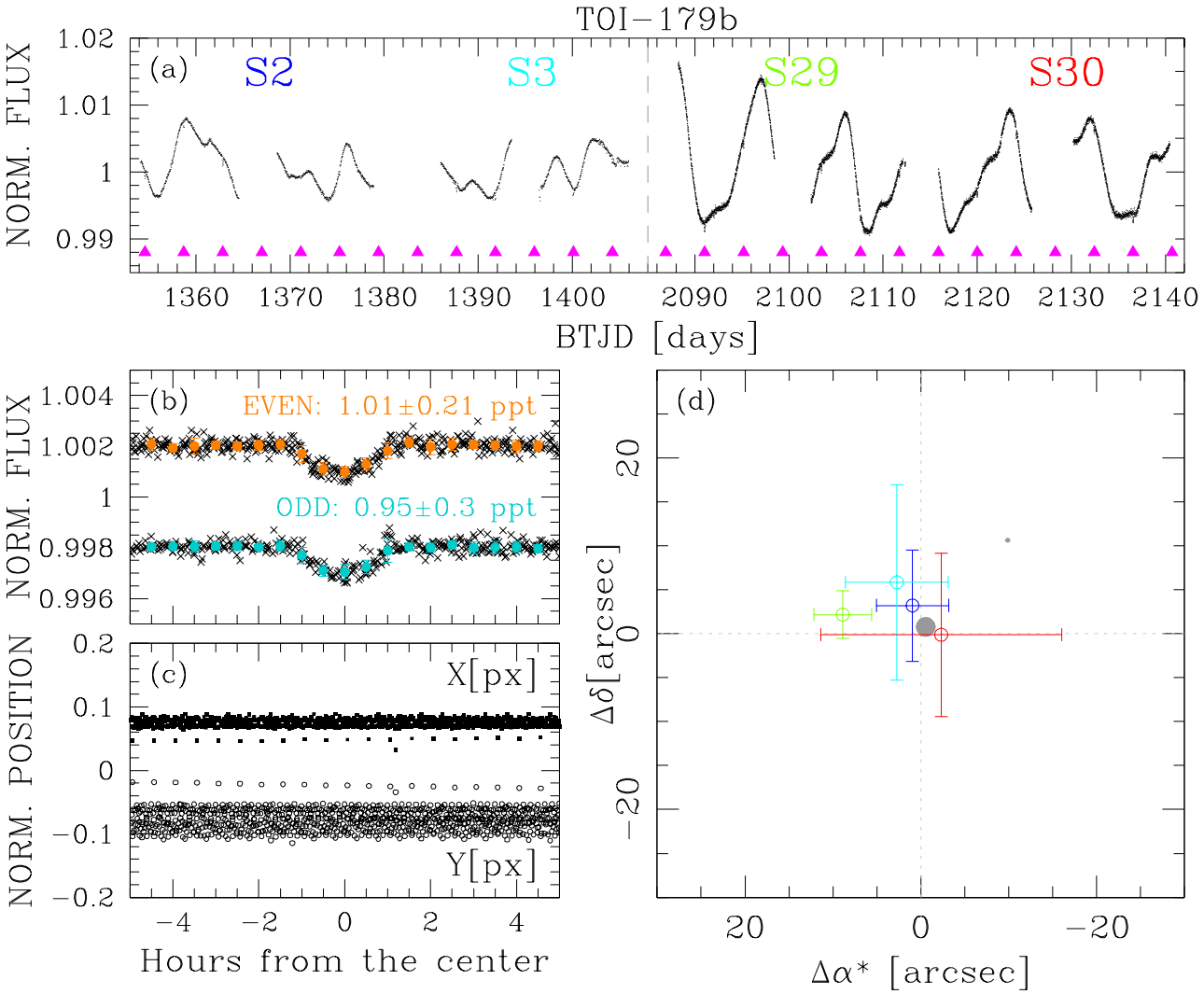

Fig. 4. Overview of the vetting tests performed for TOI-179b using the TESS data. *Panel a*: flux-normalized light curve of TOI-179 obtained using the FFIs collected during Sectors 2, 3, 29, and 30 (magenta triangles indicate the transit events). *Panel b*: comparison between phased odd (cyan) and even (orange) transits. The points are the binned phased light curves, with bins of 0.5 h. Within the errors, odd and even transits have the same depths. *Panel c*: phased X and Y-positions. There is no correlation between the positions of the star in each image and the transit signals. *Panel d*: in and out-of transit difference centroid analysis. Within 3σ the centroids correspond to the position of the star; each centroid is color-coded by sector as in *panel a*.

presence of periodic signals ascribable to stellar rotation and planetary orbit. Before running the GLS algorithm, we removed an offset and a linear long-term trend form the data, adopting the best-fit values for $\gamma_{\rm HARPS-pre}$, $\gamma_{\rm HARPS-post}$, and $\dot{\gamma}$ listed in Table 3. The results are shown in Fig. 5 (upper panel). The periodogram shows the main peak at $P = 4.34$ days, with a significantly low false alarm probability (FAP), which we derived through a bootstrap analysis. This period corresponds to the first harmonic of the stellar rotation period. Another significant peak (FAP $\sim$ 1%) is observed at a higher frequency, corresponding to the second harmonic of the stellar rotation period. Subsequently, we pre-whitened the data by removing the best-fit sinusoid model obtained with GLS, and we calculated the periodogram of the residuals (lower panel of Fig. 5). The main peak is located very close to the orbital period of the transiting companion to TOI-179 measured by TESS, and it appears to be significant (FAP = 0.3%). In summary, we obtained two results from the frequency content analysis that are useful for the more complex analysis described in Sect. 4.3: signals related to stellar activity dominate the RV time series, and the signal due to the transiting companion is already detected after pre-whitening the data.

4.3. Joint modeling of radial velocities and photometric transits

We calculated and derived the main planetary parameters of TOI-179 b by performing a fit of the combined RV+TESS short-cadence photometry dataset (sectors 2–3 and 29–30). Instead of the full TESS dataset, we used that part of the flattened light curve containing only the transit signal, and a long out-of-transit baseline (~5 h before and after the transit) to guarantee proper modeling of the photometric data. We explored the full (hyper-)parameter space using the publicly available Monte Carlo (MC) nested sampler and Bayesian inference tool MULTINEST v3.10 (e.g., Feroz et al. 2019), through the PYMULTINEST wrapper (Buchner et al. 2014). Our MC setup included 500 live points, and we adopted a sampling efficiency of 0.3. We used the code BATMAN (Kreidberg 2015) to model the photometric transits. For the RV data we modeled the time variability dominated

Table 3. Best-fit values and priors of the model parameters for the combined RV+TESS photometry fit of TOI-179 discussed in Sect. 4.3.

Parameter	Prior [a]	Best-fit value [b]	
		RV linear trend (adopted)	RV parabolic trend
Fitted			
RV stellar activity term			
h (m s^{-1})	$\mathcal{U}$(0,50)	$23.8^{+2.4}_{-2.2}$	$24.0^{+2.6}_{-2.1}$
λ (days)	$\mathcal{U}$(0,1000)	$24.0^{+6.7}_{-6.2}$	$24.1^{+6.8}_{-6.2}$
w	$\mathcal{U}$(0,1)	0.16 ± 0.03	0.16 ± 0.03
θ (days)	$\mathcal{U}$(3,10)	8.72 ± 0.04	8.71 ± 0.04
Planet-related parameters			
K_b (m s^{-1})	$\mathcal{U}$(0,50)	$11.3^{+3.3}_{-3.6}$	$11.3^{+3.4}_{-3.6}$
orbital period, P_b (days)	$\mathcal{U}$(4,4.2)	$4.1374354^{+0.0000036}_{-0.0000037}$	$4.1374355 \pm 3.6 \cdot 10^{-6}$
$T_{conj,b}$ [BJD-2450000]	$\mathcal{U}$(9111.68,9111.78)	$9111.73946^{+0.00068}_{-0.00057}$	$9111.73948^{+0.00072}_{-0.00058}$
$\sqrt{e_b}\cos\omega_{b,\star}$	$\mathcal{U}$(-1,1)	$0.56^{+0.05}_{-0.08}$	$0.56^{+0.06}_{-0.08}$
$\sqrt{e_b}\sin\omega_{b,\star}$	$\mathcal{U}$(-1,1)	$-0.025^{+0.151}_{-0.183}$	$-0.033^{+0.158}_{-0.179}$
acceleration, $\dot{\gamma}$ (m s^{-1} d^{-1})	$\mathcal{U}$(0,0.1)	0.048 ± 0.008	0.047 ± 0.011
curvature, $\ddot{\gamma}$ (m s^{-1} d^{-2})	$\mathcal{U}$(-1,1)	–	$0.4 \pm 2.2 \cdot 10^{-5}$
$R_b/R_\star$	$\mathcal{U}$(0.02,0.05)	$0.0309^{+0.0016}_{-0.0012}$	$0.0310^{+0.0016}_{-0.0012}$
inclination, i_b (deg)	$\mathcal{U}$(80,90)	$87.6^{+1.4}_{-1.0}$	$87.5^{+1.5}_{-0.9}$
RV-related parameters			
$\sigma_{jit,HARPS-pre}$ (m s^{-1})	$\mathcal{U}$(0,20)	$1.2^{+1.6}_{-0.8}$	$1.2^{+1.6}_{-0.8}$
$\gamma_{HARPS-pre}$ (m s^{-1})	$\mathcal{U}$(-100,+100)	$26.2^{+14.5}_{-14.3}$	$21.3^{+27.7}_{-27.2}$
$\sigma_{jit,HARPS-post}$ (m s^{-1})	$\mathcal{U}$(0,20)	$0.4^{+0.5}_{-0.3}$	$0.4^{+0.5}_{-0.3}$
$\gamma_{HARPS-post}$ (m s^{-1})	$\mathcal{U}$(-100,+100)	$-29.3^{+5.6}_{-5.4}$	$-30.3^{+7.8}_{-8.3}$
Light curve-related parameters			
$\sigma_{jit,TESS\ sect.\ 2-3}$	$\mathcal{U}$(0,0.001)	0.000177 ± 0.000009	0.000177 ± 0.000009
$\sigma_{jit,TESS\ sect.\ 29-30}$	$\mathcal{U}$(0,0.001)	0.000185 ± 0.000009	0.000185 ± 0.000009
LD_{c1}	$\mathcal{U}$(0,1)	$0.35^{+0.17}_{-0.20}$	$0.35^{+0.17}_{-0.20}$
LD_{c2}	$\mathcal{U}$(0,1)	$0.34^{+0.31}_{-0.24}$	$0.33^{+0.32}_{-0.23}$
Derived			
a_b (au)	–	0.0480 ± 0.0004	0.0480 ± 0.0004
e_b	–	$0.34^{+0.07}_{-0.09}$	$0.34^{+0.08}_{-0.09}$
$\omega_{b,\star}$ (rad)	–	$-0.044^{+0.284}_{-0.311}$	–0.06 ±0.03
$a_b/R_\star$ [c]	–	$14.1^{+1.0}_{-1.5}$	$14.0^{+1.1}_{-1.4}$
impact param., b	–	$0.50^{+0.12}_{-0.26}$	$0.51^{+0.11}_{-0.28}$
transit duration, $T_{1,4}$ (days)	–	$0.0860^{+0.0051}_{-0.0053}$	$0.0861^{+0.0056}_{-0.0051}$
radius, R_b ($R_\oplus$)	–	$2.60^{-0.13}_{+0.15}$	$2.60^{+0.15}_{-0.13}$
mass, m_b ($M_\oplus$)	–	$24.1^{+7.1}_{-7.7}$	$24.0^{+7.3}_{-7.6}$
mean density, ρ_b (g cm^{-3})	–	$7.5^{+2.6}_{-2.4}$	$7.4^{+2.7}_{-2.5}$
Surface gravity, g_b (m s^{-2})	–	35 ± 11	35 ± 11
Log. Bayesian evidence, ln $\mathcal{Z}$		13971.5	13961.3

Notes. [a]$\mathcal{U}$ denotes a prior drawn from an uninformative distributions. [b]Parameter uncertainties are given as the 16th and 84th percentiles of the posterior distributions. [c]We used the stellar density ρ_* [$\rho_\odot$] as a free parameter with prior $\mathcal{N}$(1.9,0.2), from which we derived $a_b/R_\star$ at each step of the MC sampling. We recovered the prior distribution in the posterior of ρ_*.

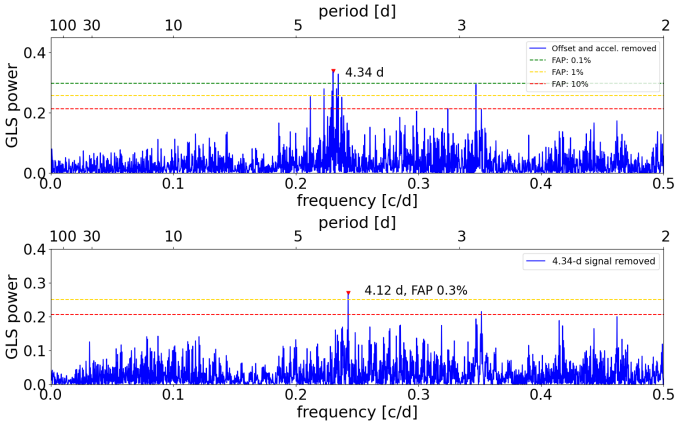

Fig. 5. GLS periodograms of the RVs. After removing the long-term acceleration from the original data (upper panel); after removing the best-fit sinusoid calculated by GLS from the pre-whitened data (lower panel). Frequencies (bottom axis) and periods (top axis) are both shown on the x-axis. Bootstrap-derived FAPs are indicated by horizontal dashed lines.

by stellar activity modulations by means of a Gaussian process (GP) regression, and adopting a quasi-periodic (QP) kernel. We used the publicly available PYTHON module GEORGE v0.2.1 (Ambikasaran et al. 2015) to perform the GP regression within the MultiNest framework. The elements of the QP covariance matrix (e.g., Haywood et al. 2014) implemented in our model is defined as follows:

$$k_{\rm QP}(t,t') = h^2 \cdot \exp\left[-\frac{(t-t')^2}{2\lambda^2} - \frac{\sin^2(\pi(t-t')/\theta)}{2w^2}\right] + (\sigma^2_{\rm RV}(t) + \sigma^2_{\rm jit,\,RV}) \cdot \delta_{t,t'}. \quad (1)$$

Here t and t' represent two different epochs of observations, $\sigma_{\rm RV}$ is the radial velocity uncertainty, and $\delta_{t,t'}$ is the Kronecker delta. Our analysis takes into account other sources of uncorrelated noise (instrumental and/or astrophysical) by including a constant jitter term $\sigma_{\rm jit,\,RV}$, which is added in quadrature to the formal uncertainties $\sigma_{\rm RV}$. The GP hyper-parameters are h, which denotes the scale amplitude of the correlated signal; θ, which represents the periodic timescale of the modeled signal and corresponds to the stellar rotation period; w, which describes the weight of the rotation period harmonic content within a complete stellar rotation (i.e., a low value of w indicates that the periodic variations contain a significant contribution from the harmonics of the rotation periods); and λ, which represents the decay timescale of the correlations and is related to the temporal evolution of the magnetically active regions responsible for the correlated signal observed in the RVs. When fitting the RVs we introduced two offsets ($\gamma_{\rm pre}$ and $\gamma_{\rm post}$) and white noise jitters (σ_{pre} and $\sigma_{\rm post}$) for the pre- and post-fiber upgrade datasets. For the modeling of the TESS transit light curve, we adopted a limb darkening (LD) quadratic law, with uniform priors on the LD coefficients $\rm LD_{c1}$ and $\rm LD_{c2}$. We fitted constant jitter terms $\sigma_{\rm jit,\,TESS}$ in quadrature to the formal photometric uncertainties, one jitter for data collected in sectors 2–3 and another for data from sectors 29–30, to take into account variations in TESS performance over 2 yr of operation. We modeled the orbit of planet b with a Keplerian, adopting the parameterization $\sqrt{e_{\rm b}}\cos\omega_{\rm b,\star}$ and $\sqrt{e_{\rm b}}\sin\omega_{\rm b,\star}$ instead of using $e_{\rm b}$ and $\omega_{\rm b,\star}$ as free parameters. We included an acceleration $\dot\gamma$ to model the long-term trend that dominates the RV time series, and also tested a parabolic long-term trend by including the additional free parameter $\ddot\gamma$.

The results of the GP regression are shown in Fig. 6; the priors and best-fit values for all the free (hyper-) parameters used in our model are summarized in Table 3, while the cornerplots of the resulting distributions and correlations of each parameter are shown in Appendix C. Our results show that the model including a linear long-term trend in the RVs is statistically much more favored over a model with a quadratic trend ($\ln\mathcal{Z}_{\rm linear} - \ln\mathcal{Z}_{\rm quadr.} = +10.2$, where $\mathcal{Z}$ represents the Bayesian evidence), excluding the presence of a significant curvature in the RVs. The RV signature of the transiting planet is detected with a 3.3σ confidence ($K = 11.3^{+3.3}_{-3.6}\,{\rm m\,s^{-1}}$), corresponding to a mass $m_{\rm b} = 24.1^{+7.1}_{-7.7}\,M_\oplus$, indicating a rather compact structure for the planet. The planetary orbit is eccentric with a 3.8σ significance ($e_b = 0.34^{+0.07}_{-0.09}$). These properties are further discussed in Sect. 6. Figures 7 and 8 show the corresponding best-fit spectroscopic orbit of TOI-179 due to planet b, and the transit light curve of TOI-179 b.

We note that the results for the GP part of the RV model can be considered realistic and trustworthy. The stellar rotation period θ is precisely recovered even using a quite broad uninformative prior; the short decay timescale λ, equivalent to about three rotation cycles (see Fig. C.1), is supported by the result we obtained after applying a GP quasi-periodic regression to the TESS photometry of sectors 2–3 and 29–30, modeled separately and with transit signals removed. We found $\lambda \sim 10$ days in both cases, showing that the evolutionary timescale of the active regions is indeed on the order of a few stellar rotational periods. It must be taken into account that the TESS and RVs measurements are not contemporaneous, hence the stellar activity behavior cannot be compared directly in the two datasets, and is why we could not use the photometry to directly constrain the activity term in the RV model. Moreover, the two datasets have very different sampling; therefore, we cannot expect to find the same values of λ, but only to verify that the order of magnitude is similar to support the result for the RVs, as happens in this case.

5. New low-mass companion at close separation detected with SPHERE

A close companion is clearly identified at $S/N = 14$ in the non-coronagraphic SPHERE datasets obtained at both epochs (2019 October 11 and 2019 December 18) at a projected separation of 84.5±3.6 mas and position angle 212.0±1.5 deg (Fig. 9). This is the average value obtained at the two epochs; they are fairly close in time, so we do not expect significant orbital motion between them. The magnitude differences with respect to HD 18599 are 6.42 ± 0.07 mag in J band and 6.05 ± 0.07 mag in H band[3] (internal errors only). These values correspond to absolute magnitudes of $M_{\rm J} = 10.91 \pm 0.07$ and $M_{\rm H} = 10.14 \pm 0.07$ mag. For the adopted age of 400 ± 100 Myr, the application of Baraffe et al. (2015) models yields a mass of $83^{+4}_{-6}\,M_J$. The observed $J - H$ color (0.77±0.10) implies a spectral type between very late M to early L, in agreement (although less constraining in terms of mass) to the estimate provided above from the absolute magnitudes.

The object is not detected in the NaCo images, as expected from the contrast limits shown in Fig. 3. For the same reason, it

[3] This H band actually only includes the wavelength range accessible to the SPHERE IFS between 1.50 and 1.65 µm, and it is thus not coincident with the usual definition.

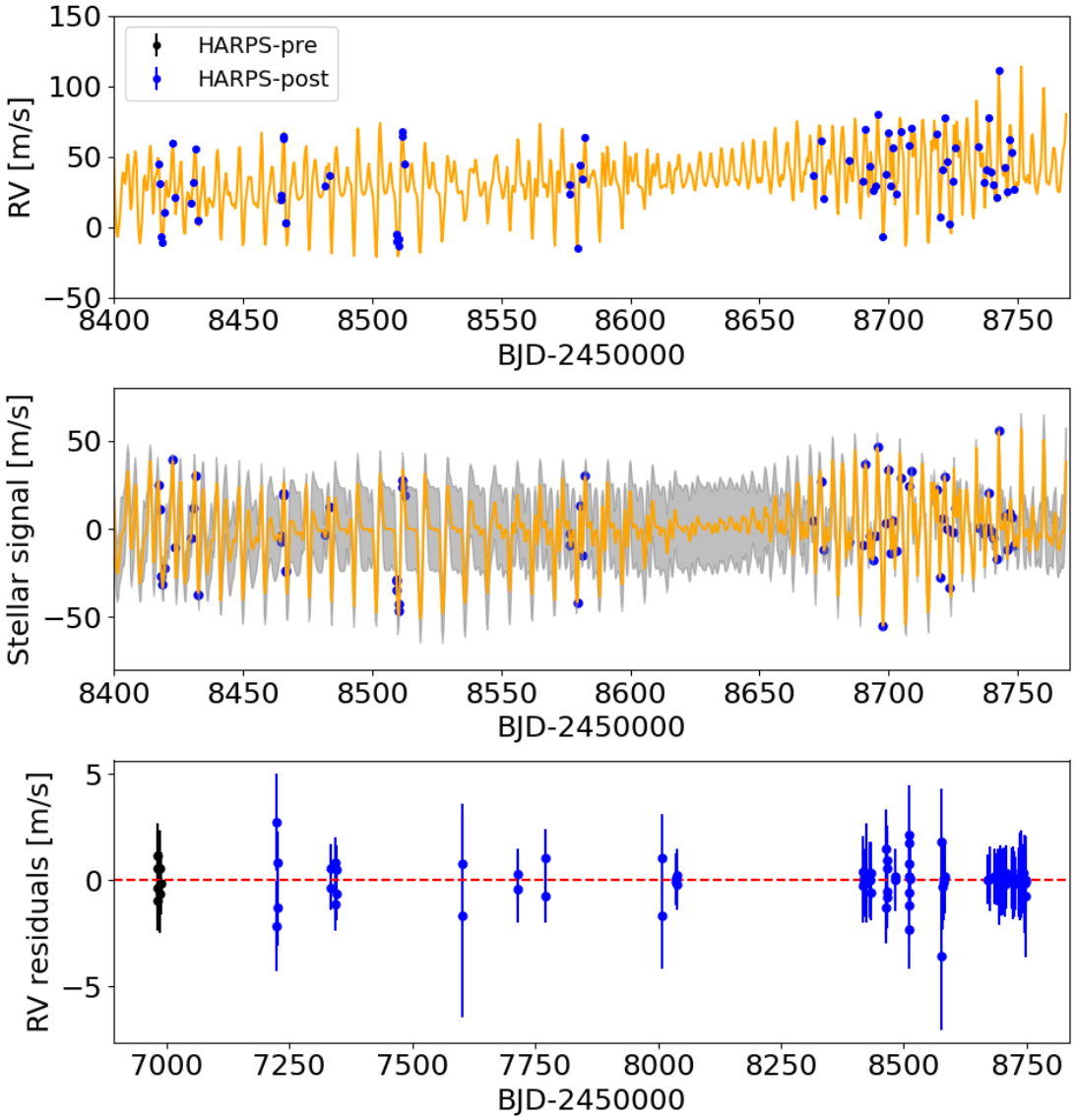

Fig. 6. Best-fit results of the joint RV+TESS short-cadence light curve (Table 3). *Top panel:* original RVs with offsets removed (only HARPS-post RVs are shown for clarity). *Middle panel:* quasi-periodic stellar activity term (only HARPS-post RVs are shown for clarity). *Bottom panel:* RV residuals. The RV have been extracted with the pipeline TERRA, and error bars include the uncorrelated jitter terms added in quadrature to the formal uncertainties. The orange lines indicate the best-fit models: Keplerian+linear trend+stellar activity (top); stellar activity (middle). The gray shaded area in the middle panel gives the $\pm 1\sigma$ uncertainty of the quasi-periodic activity signal.

remains undetected in shallower imaging of TOI-179 published by Ziegler et al. (2020).

The physical association with the central star is not fully demonstrated as the time baseline between the two SPHERE observations is too short for the common proper motion test. However, we note that a stationary background object would be expected to lie at a projected separation of 203 mas from the central star at the epoch of the NaCo observations, above our detection limits (Fig. 3) for reasonable $H - L$ colors of the object[4]. This does not rule out a non-stationary background object with intrinsic proper motion (Nielsen et al. 2017) keeping the projected separation smaller in 2016, but this option has a very low probability of occurring.

If we also consider the existence of the RV trend and astrometric signature (see below), which are compatible with the source detected in imaging and the observed very red color, in the following we consider the object to be a physical companion, either a very low-mass star or a high-mass brown dwarf, mostly depending on the stellar age. We labeled it HD 18599 B[5].

5.1. Origin of the long-term RV trend of TOI-179

As shown in Sect. 4.3, the RV time series shows a clear long-term trend with a slope of $17.5 \pm 2.9\,\mathrm{m\,s^{-1}\,yr^{-1}}$. Figure 10 shows the RV residuals, after removing the signal due to TOI-179 b,

[4] A field object with blue colors is ruled out by the observed colors measured on the SPHERE data.

[5] The wide companions CD-56 593A and B had not been identified as HD 18599 B and C in SIMBAD at the time of writing, although Mugrauer & Michel (2020) label the unresolved entry (from *Gaia* DR2) as TOI-179BC. WDS instead labels CD-56 593A and B as WDS 02570-5613A and B, respectively, and HD 18599 as WDS 02570-5613C, even though this last is the brightest and most massive component in the system. We propose identifying the CD-56 593 components as HD 18599 C and D to avoid ambiguities.

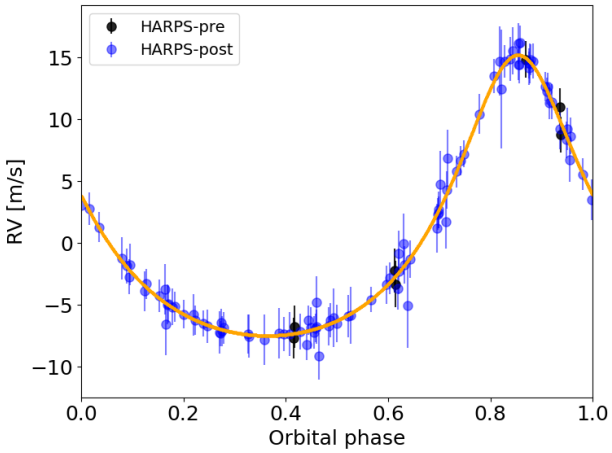

Fig. 7. Spectroscopic orbit of TOI-179 due to planet b. The best-fit model is indicated by an orange line.

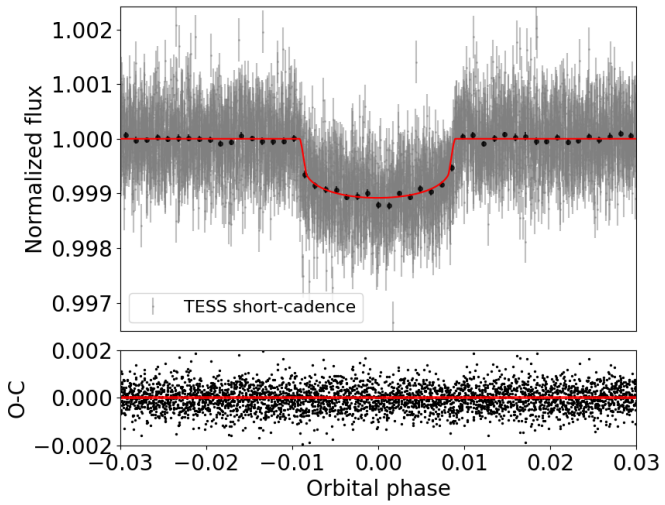

Fig. 8. Best-fit transit signal of TOI-179 b based on TESS short-cadence photometry (Table 3). Model residuals O–C are shown in the bottom panel.

with and without the quasi-periodic activity signal modulated over the stellar rotation. The inclusion of a quadratic term is not highly significant (Table 3).

We note that the activity indices, in particular the Hα index measurements, also show a possible long-term trend (Appendix A.5). While it is possible that this also contributes to some extent to the long-term signal seen in the RV time series, we found that the companion revealed in imaging and the astrometric signature (Sect. 5.2), and the amplitude itself of the RV trend, are much larger than the typical RV signatures of activity cycles (Lovis et al. 2011; Carolo et al. 2014), which strongly argues for a Keplerian origin of the observed RV trend. Moreover, this assumption is supported by the lack of a long-term trend in the BIS diagnostic (Fig. A.3, lower-right panel), which instead shows the anti-correlation with RVs typically observed in active late-type stars and the significant periodicity corresponding to rotational modulations.

Nonetheless, we quantified a possible overestimate on the measured RV acceleration $\dot{\gamma}$ due to the long-term activity by repeating the fit described in Sect. 4.3; we carried out two tests using the spectroscopic activity diagnostics based on the Hα and calcium lines (Appendix A.5). In the first test, we included a

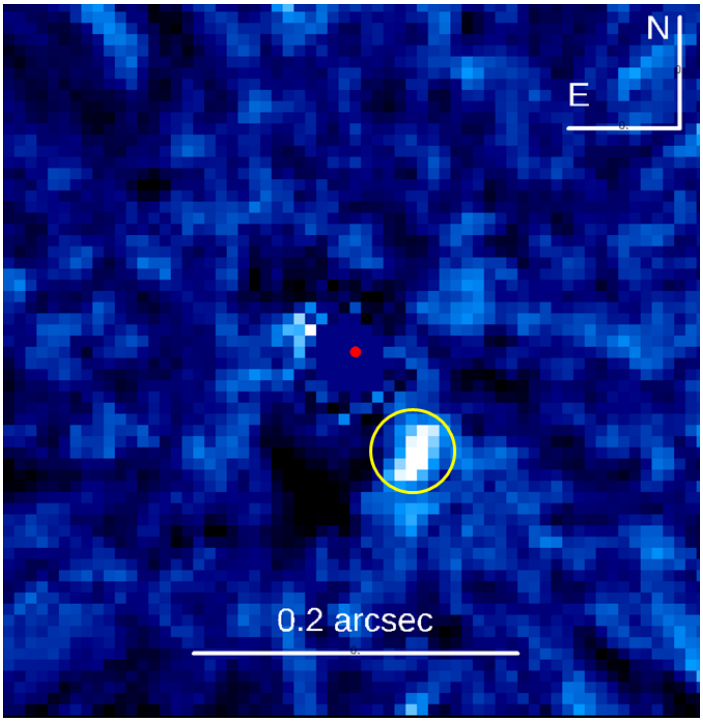

Fig. 9. Detection of the low-mass companion in the non-coronagraphic SPHERE images (average of the two epochs). The red dot gives the position of the star and the yellow circle shows the companion. The star image was subtracted using the differential approach described in the text. The small elongation of the detected source is due to the subtraction between the images taken at different angles, in a similar way to the classic ADI pattern.

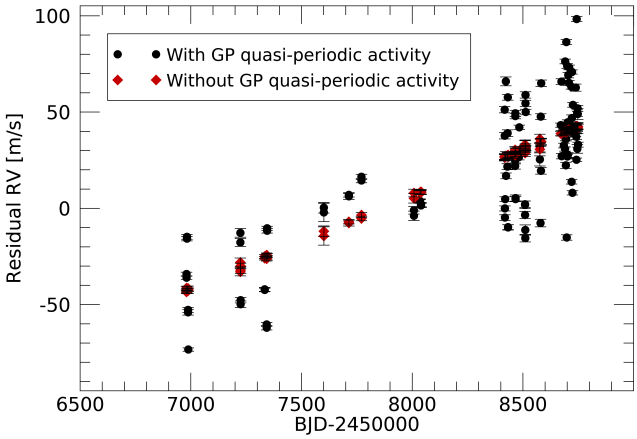

Fig. 10. Residuals of the HARPS RVs. Black dots: After removing the best-fit spectroscopic orbit of TOI-179 b while keeping the activity signal. Red diamonds: After also removing the GP quasi-periodic activity signal.

linear term with the Ha16 index in the model to correct for a RV–activity diagnostic correlation. We used large and uninformative priors for the coefficients of the linear model, and we obtained $\dot{\gamma} = 0.042^{+0.009}_{-0.008}$ m s^{-1} day^{-1}, slightly less than but in agreement with the previous estimate (0.048 ± 0.008 m s^{-1} day^{-1}), without changes in the values planetary parameters.

In the second test we considered a more complex model, consisitng of 28 free parameters, including the time series of the S index. The model includes a linear term with the S-index to correct for a RV–activity diagnostic correlation; since the

rotational modulation is detected in the S index periodogram (Appendix A.5), we also include a GP quasi-periodic correlated term to model the S index time series, together with a quadratic long-term trend. Except for the scale amplitude h of the GP, the three hyper-parameters left (λ, w, and θ) are shared between the activity diagnostic and RVs. We found $\dot{\gamma} = 0.047^{+0.008}_{-0.009}$ m s^{-1} day^{-1}, in agreement with the previous estimate, without changes in the values of the planetary model parameters. We note that the best-fit values of the stellar rotation period θ and that of the evolutionary activity timescale λ are perfectly consistent with those obtained by fitting the RVs alone, showing that a GP quasi-periodic trained on the S index does not improve or even change the best-fit solution for the activity signal present in the RVs. Hence we conclude that the observed long-term RV trend is mostly of Keplerian origin and assume in the following that it is due to HD 18599 B. Finally, the trend cannot be due to secular acceleration (Zechmeister et al. 2009) as this effect is removed by the TERRA pipeline when deriving the RVs.

5.2. Astrometric signatures

Kervella et al. (2022) detected a rather large proper motion anomaly (PMA) of 0.406 ± 0.036 mas yr^{-1} at a position angle of 265.54 degree by comparing the proper motion measured by *Gaia* eDR3 with the long-term proper motion obtained comparing the position of TOI-179 at the *Gaia* eDR3 epoch (J2016.0) with that obtained at the Hipparcos epoch (J1991.25). This large PMA (detected with a highly significant S/N of 11.4) is clearly indicative of an acceleration due to a companion. This cannot be attributed either to the transiting planet or to the wide companions CD-56 593 A and B; it may instead be ascribed to the low-mass companion observed by SPHERE (HD 18599 B), further supporting the high detection efficiency for this kind of object around stars with significant PMA (Bonavita et al. 2022a). We note that the PMAs measured at the Hipparcos epoch are −0.511 ± 0.720 and −0.301 ± 0.690 mas yr^{-1} in right ascension and declination, respectively. These values are not significant, but comparable with the result obtained at the *Gaia* epoch.

5.3. Constraints on the orbit of HD 18599 B

We used the astrometric epochs obtained with SPHERE, the RV long-term trend, and the proper motion anomaly signatures at both Hipparcos and *Gaia* epochs to constrain the orbit of HD 18599 B.

As a first qualitative guess, we infer that the object is caught at a projected separation much smaller than the physical semimajor axis. A strong RV signal ($K \sim 1$ km s^{-1} for edge-on orbit) of period ∼3.6 yr is expected for a companion with semimajor axis equal to the 3.3 au projected separation of HD 18599 B. Instead, we observe a monotonic behavior of the RVs over 4.8 yr (upward trend), with no significant power at 3–5 yr in the periodogram. A very small RV amplitude can be explained with a pole-on orbit, but in this case the astrometric motion should be roughly perpendicular to the projected separation, which is very different from the observed *Gaia* proper motion anomaly.

For a quantitative analysis, we first used the program ORBIT (Tokovinin 2016)[6] as a tool to find possible orbital solutions compatible with the observational data, fixing the total mass for the system obtained considering the mass of the star and of the companion derived from photometry. We explored the period range from 3 to 150 yr (the small apparent separation of the SPHERE detections makes longer periods unlikely). While there are not enough data to completely define this orbit, various constraints can be obtained. In general, we found two families of orbital solutions compatible with the observational data, either with periods shorter than about 30–40 yr or with periods longer than 60–80 yr, while orbits with intermediate periods (roughly twice the separation between HIPPARCOS and *Gaia* observations) are excluded.

In the case of short periods, the small separation of the companion detected by SPHERE and the shallow almost linear trend on the RV curve over a quite long range of 5 yr point towards a highly eccentric orbit ($e \gtrsim 0.9$) seen at high inclination ($i \sim 100$ degree) and with an angle between the periastron and the line of nodes ω not too far from 90 degrees (the longer the period, the closer this condition). The mass for HD 18599 B should be small (between 20 and 40 $M_{\rm Jupiter}$), which is essentially a consequence of the observed shallow trend in radial velocities. This is incompatible with the value derived from photometry.

On the other hand, orbits belonging to the long-period family have moderate eccentricity ($e \sim 0.5$), an even higher inclination ($i \sim 95$ degree), and a wider range of values for ω. The mass of HD 18599 B found with these orbits is in the range 60–120 $M_{\rm Jupiter}$, compatible with the value indicated by photometry. If we use this last as a prior, the orbital period is constrained to be not too far from 100 yr.

The two orbit families also correspond to very different values for the periastron distance. The short-period orbits have very short periastron (around or less than 1 au); the long-period orbits have much larger values (between 7 and 14 au). This leads to a very different strength of the dynamical interaction between the secondary and the transiting planet. We note that for the orbit of the transiting companion to be stable, the periastron distance for HD 18599 B should be larger than ∼0.24 au, requiring the eccentricity to be lower than 0.97 for short-period orbits, and a bit higher for long-period ones. Finally, the very high value of the inclination suggests that the orbit of HD 18599 B might be nearly co-planar with that of the transiting planet.

Next, we explored the parameter space of possible solutions using a Bayesian analysis of the combined RV and absolute and relative astrometry observations using a differential evolution Markov chain Monte Carlo (DE-MCMC) method (Ter Braak 2006; Eastman et al. 2013). As described in detail in Drimmel et al. (2021), the combination of the three types of datasets allows us to directly determine the mass ratio q. By placing narrower and broader uniform priors on the orbital period (P in the range [3., 60.] yr and [3., 200.] yr, respectively) we reproduced in general terms the solutions obtained with the ORBIT package. By adopting an additional, indirect prior on the system distance based on the knowledge of the *Gaia* eDR3 parallax (Bailer-Jones et al. 2021), the shorter-period solution converged (based on the Gelman-Rubin statistics; see, e.g., Ford 2006) to $P \sim 45$ yr, $e \sim 0.89$, $q \sim 0.092$. The derived inclination is found to be $i \sim 85$ deg. Given the primary mass reported in Table 2, the inferred companion mass is $M_B \sim 82\,M_{\rm J}$. The equivalent set of values for the parameters of the longer-period solution is $P \sim 119$ yr, $e \sim 0.32$, $q \sim 0.059$, $i \sim 73$ deg, and $M_B \sim 53$ M$_J$. The long-period solution is represented graphically in Fig. 11.

It should be noted that the long-period solution is clearly favored in terms of likelihood ($\Delta \ln \mathcal{L} > 10$). Nevertheless, it is also clear that the essentially single epoch for imaging data and the long-term trend in RVs make any robust inference on the exact orbital configuration and mass of HD 18599 B unfeasible. The above numbers should be considered simply representative of the two broad families of orbits, and the

[6] https://zenodo.org/record/61119#.Xg83GxvSJ24

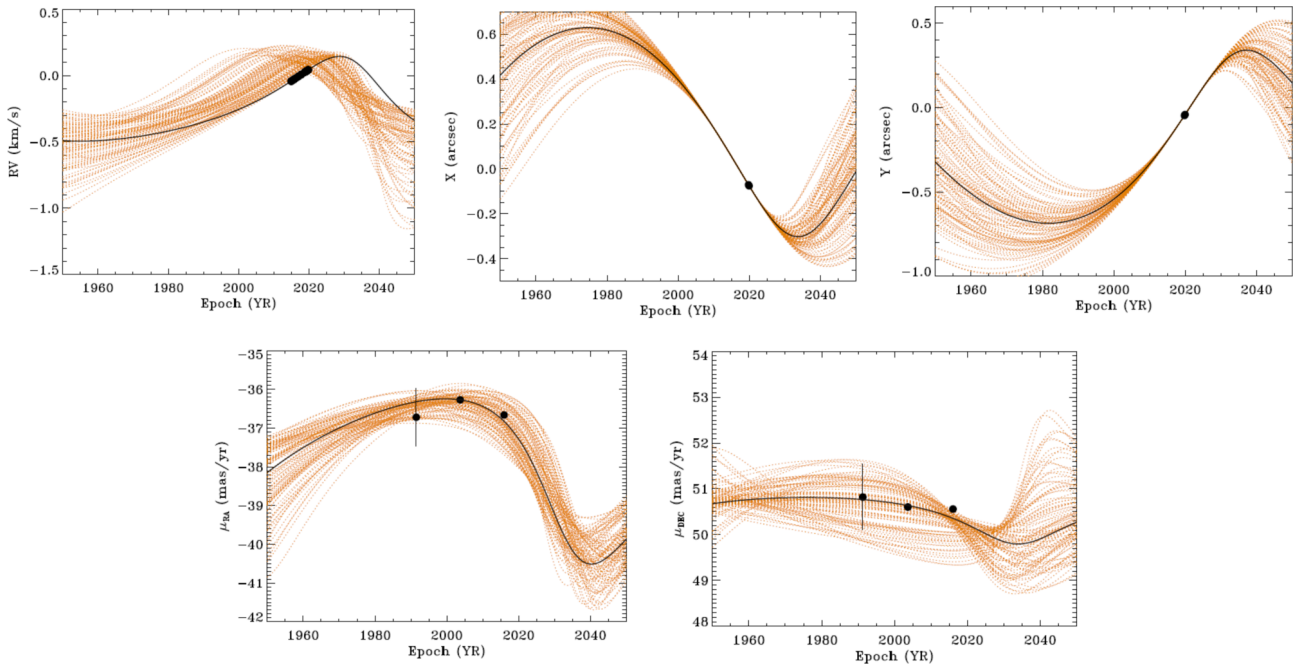

Fig. 11. RV, sky position, and motion on the sky for the long-period solution resulting from the MCMC described in the text. The black line shows the nominal best-fit solution. The dashed orange lines represent a random selection of orbital solutions drawn from the posterior distributions of the model parameters from the DE-MCMC analysis. The black dots are the observational data from HARPS (RV panel), SPHERE (X and Y panels), and *Gaia* and HIPPARCOS (proper motion panels).

corresponding approximate companion masses, that are allowed given the observational constraints at hand: a) shorter period, very high eccentricity, almost edge-on configuration, and b) longer period, lower-eccentricity, still highly inclined configuration.

5.4. Ruling out HD 18599 B as host of transit

The presence of a close companion around TOI-179 means that we need to evaluate the idea that observed transits do not occur on the central star and that HD 18599 B is a diluted eclipsing binary (see, e.g., Torres et al. 2004). This hypothesis is dismissed for a number of reasons. On the one hand, the expected magnitude difference between TOI-179 and HD 18599 B in V band is more than 12 mag (using the models by Baraffe et al. 2015), making the contamination of the HARPS spectra negligible. Therefore, the presence of a Doppler signal with the same period and phase of the photometric cannot be ascribed to HD 18599 B. On the other hand, the photometric properties of the transits (depth, duration, and shape) are also not compatible with diluted eclipses occurring on the low-mass companion.

6. Discussion

6.1. Architecture of TOI-179 system

The architecture of TOI-179, with a close-in low-mass transiting planet in eccentric orbit and an outer companion with mass close to the stellar–substellar boundary and possibly coplanar with the transiting planet, is fairly unusual in the wide zoo of known planetary systems.

Few examples are found of low-mass planets in close orbits with outermost companions (brown dwarfs or very low-mass stars) within a few dozen au. The M dwarf GJ 229 is well known for hosting the first T-type companion discovered by Nakajima et al. (1995). More recently, two low-mass planet candidates were claimed through RVs by Tuomi et al. (2014), one of which (GJ 229 c, $m \sin i$ 7 $M_\oplus$, period 122 d, eccentricity 0.19) was confirmed via further observations by Feng et al. (2020). As this planet is non-transiting, the relative inclination with respect to the BD orbit is unknown. The orbit of the BD has a semimajor axis of 34.7 au and is highly eccentric (0.846±0.015, Brandt et al. 2020). Among the planet hosts with very low-mass stellar companions (mass $\leq 0.1 M_\odot$) at close separation ($\leq$ 100 au) we mention only three cases listed in the catalogs by Thebault & Haghighipour (2015)[7] and Schwarz et al. (2016)[8]. The G dwarf GJ 3021 has a 0.09 $M_\odot$ star at 68 au (projected separation; Chauvin et al. 2006) and a moderately massive giant planet ($m \sin i$ 3.4 M_J) at 0.5 au. K2-126 is a K7V Hyades member with three low-mass transiting planets (Mann et al. 2018) and a 0.10 $M_\odot$ stellar companion at a projected separation of 40 au (Ciardi et al. 2018). Finally, HD 42936 is an exceptionally compact system, formed of a low-mass planet (which is possibly evaporating) very close to the K0 central star and a 0.076 $M_\odot$ star (minimum mass from RV solution) with semimajor axis 1.22 au and eccentricity 0.59 (Barnes et al. 2020). Thus, the stability zone around the primary extends only up to 0.16 au. This architecture is qualitatively similar but more extreme than the high eccentricity case for the TOI-179 system described above.

TOI-179 then represents one of the few known cases of a star hosting at least one planet and a second companion (a very low-mass star or BD) in close orbit, making it an interesting laboratory for our understanding of formation of both these kinds of objects in the same system. The characteristics of TOI-179b (see also below) suggests a formation path through the core-accretion mechanism (e.g., Mordasini et al. 2012), while HD18599 B

[7] Updated version at http://exoplanet.eu/planets_binary/
[8] Updated version at https://www.univie.ac.at/adg/schwarz/multiple.html

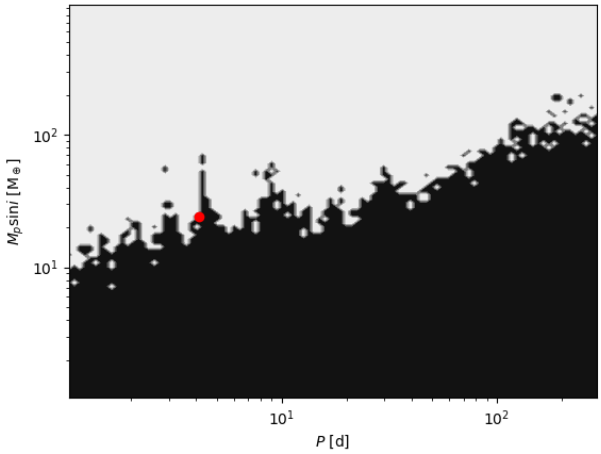

Fig. 12. Detection function map of the RV time series of TOI-179. The white part corresponds to the area in the period–minimum mass space where additional signals could be detected if present in the data, while the black region corresponds to the area where the detection probability is negligible. The red circle gives the position in the parameter space of the transiting planet TOI-179b.

might be the outcome of disk fragmentation (Stamatellos & Whitworth 2009). The likely coplanar orbits and eccentric orbit for the outer companion add further constraints on the processes of formation and evolution, although the ambiguities on the orbit of HD 18599B do not allow conclusive inferences.

The presence of the other two companions CD-56 593 A and B should be mentioned as a potential source of dynamical interactions in the system, although their current projected separation (3400 au) is very large. Rearrangement of the configuration of the system may have occurred in the past (see, e.g., Marzari & Barbieri 2007; Kaib et al. 2013) or the orbit may be highly eccentric, although these hypotheses remain speculative.

6.2. Constraints on additional companions

Photometric, spectroscopic, and adaptive optics (AO) data do not provide indications for additional companions except for the transiting planet TOI-179b and the imaged low-mass object HD 18599 B.

In greater detail, from the RV time series we can derive the detection limits for additional RV objects, following the Bayesian technique described in Pinamonti et al. (2022) , adopting the results from the joint modeling of RVs and photometric transits as priors on the TOI-179b planetary signal. The resulting detection function map is shown in Fig. 12. We can rule out the existence of planetary companions with $m \sin i$ larger than 28 and 80 $M_\oplus$ with orbital periods of about 10 and 100 days, respectively.

We also used the coronagraphic data described in Sect. 2.3.1 to obtain a final image of the FoV around TOI-179. No obvious point source was identified in the IFS or in the IRDIS FoV. We used the contrast limits derived in Sect. 2.3.1 and shown in Fig. 2 to define the mass limits for both the epochs and for both the SPHERE instruments assuming an age of 400±100 Myr and using the AMES-COND models (Allard et al. 2003). The results of this procedure are displayed in Fig. 13 where we can see that at separations from the host star lower than ∼20 au we can exclude companions with a mass on the order of 10 $M_{\rm Jup}$ while at separations larger than 50 au we can exclude companions with masses higher than 3–4 $M_{\rm Jup}$. The lack of additional companions is not surprising considering the presence of HD 18599B

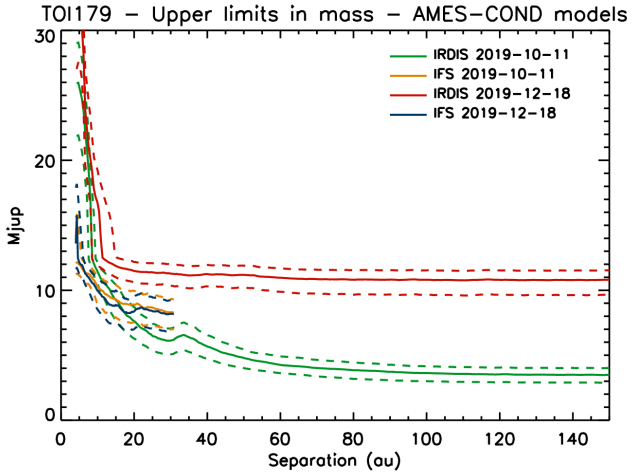

Fig. 13. Mass detection limits expressed in $M_{\rm Jup}$ as a function of the separation for both epochs, and for IRDIS and IFS. The dashed lines represent the possible mass ranges due to the age uncertainty.

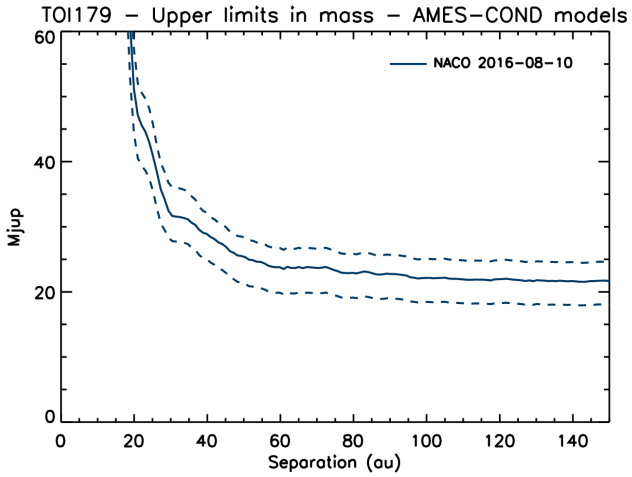

Fig. 14. Mass detection limits expressed in $M_{\rm Jup}$ as a function of the separation obtained from the NACO data. The dashed lines represent the possible mass ranges due to the age uncertainty.

at a projected separation much smaller than the true semimajor axis, with indications for an eccentric orbit.

The same procedure was also performed to infer the mass detection limits from the NaCo data (Sect. 2.3.2). The results are displayed in Fig. 14. As expected, the mass limits that we obtain in this case are much higher than those obtained with SPHERE.

6.3. Dynamical interactions

While the lack of a well-defined orbit for the outer companion does not allow us to address in depth the occurrence of dynamical interactions between the objects in the system, we performed some explorative evaluations and considered representative solutions for the two families of possible orbits identified in Sect. 5.3.

The close distance of the planet to the primary star ensures long-term stability to the system in both configurations in spite of the presence of the low-mass companion. Due to the plausible high value of eccentricity of the massive companion and of the planet it is not possible to apply the Laplace–Lagrange secular theory. The amplitude of the eccentricity oscillations of the planet has been numerically evaluated to be on the order

of 0.1–0.2 for the first configuration with a period of $\sim 10^5$ yr, depending on the initial values of the orbital angles, and on the order of 0.04–0.08 for the second configuration with periods on the order of $\sim 10^7$ yr. As a consequence, the high eccentricity value of the planet is not due to the secular perturbations, but it is potentially related to an earlier phase of dynamical instability (planet–planet scattering). The Kozai mechanism appears unlikely considering the probable configuration close to coplanarity of the planet and low-mass companion. It is possible that a second planet was present in the system and it was scattered out of the system leaving the observed planet in an excited orbit.

In the first configuration, the fast secular oscillations may prevent the tidal circularization of the orbit, while the second configuration appears to be more responsive to tidal forces due to the smaller secular oscillations and their longer period. The high eccentricity of HD 18599 B in the first configuration may not be primordial and even in this case a chaotic origin may be invoked. A period of dynamical instability involving the outer stars may have driven the object closer to the primary after the scattering of an additional star.

6.4. Tidal evolution and the origin of the eccentricity of TOI-179b

The moderately high eccentricity of TOI-179b ($0.34^{+0.07}_{-0.09}$) is unusual among planets with measured eccentricities. Correia et al. (2020) found that planets with radii between 3 and 9 $R_\oplus$ have small but significant eccentricities (typically ~0.15). High eccentricities are instead less common for planets below 3 $R_\oplus$, although the data are rather sparse. The only other known transiting planet with radius <9 $R_\oplus$, period shorter than 5 days, and eccentricity higher than 0.3 is TOI-942b (Carleo et al. 2021), although the measurement suffers from large uncertainty. The case of TOI-942b, however, appears to be different as there is another close-in low-mass transiting planet (TOI-942c) with a period of 10.2 days, while TOI-179 has a more massive companion at the BD–low-mass star boundary at much wider separation. Furthermore, the star TOI-942 is younger (50 Myr).

In order to shed light on the origin of the moderately high eccentricity, we estimated the timescale of tidal circularization, which depends mainly on the tidal modified quality factor Q'_p of the planet, the role of tidal dissipation inside the star being much less important, even when we assume a dynamical tide produced by inertial waves during most of the past evolution of the system, given that the rotation period of the host star is close to twice the orbital period (Ogilvie 2014). The value of Q'_p is highly uncertain because it depends on the internal stratification and composition of the planet. Assuming that tidal dissipation occurs mainly in a rocky and/or icy structure, $Q'_p \approx 10^3$ (see Tobie et al. 2019; Lanza 2021) and the circularization timescale is on the order of ≈ 50 Myr. Nevertheless, given the uncertainty regarding the internal structure of the planet and consequently on its rheology, it is important not to overinterpret this estimate. An upper limit to the circularization timescale may be found by assuming $Q'_p \approx 10^5$, characteristic of a giant planet where most of the tidal dissipation occurs in fluid layers (Ogilvie 2014, Sect. 5.4), which is likely not the case for TOI-179b. In this case, the eccentricity of TOI-179b can be a remnant of its formation and migration processes because the estimated circularization timescale is ~4 Gyr. All these estimates are based on the constant time lag tidal model of Leconte et al. (2010), where the transformation between the modified tidal quality factor and the time lag is made through their Eq. (19). On the other hand, the low-mass companion HD 18599 B might also be involved, pumping the eccentricity of the transiting planet through dynamical interactions, as discussed in Sect. 6.3.

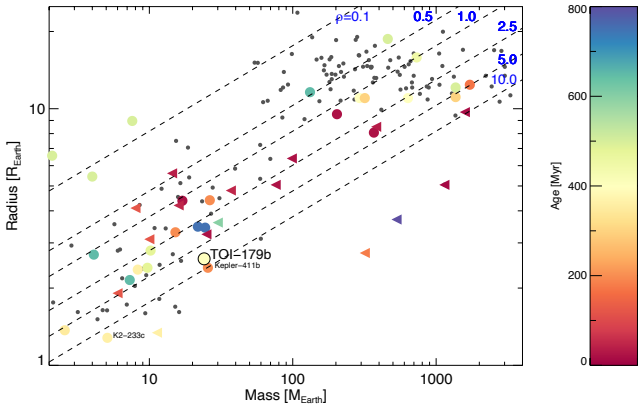

Fig. 15. Mass–radius diagram of the well-characterized exoplanet population (gray dots) and of the young transiting planets as a function of stellar age (see color-code on the right). The colored circles indicate planets with measured, mass while triangles indicate planets with mass upper limit only. The dashed lines represent the loci of equal density (g cm^{-3}).

Independently of its origin, the eccentric orbit is expected to lead to a pseudosynchronous rotation of the planet with a rotation period ~1.7 times shorter than the orbital period and an internal tidal dissipation P_{diss} that ranges from 2×10^{18} to 2×10^{20} W for $e = 0.34$ and Q'_p ranging from 10^5 to 10^3 (P_{diss} is directly proportional to e^2 and inversely proportional to Q'_p; see Miller et al. 2009). The estimated surface heat flux ranges between ≈150 and $\approx 5 \times 10^4$ W m^{-2}, which is hundreds or thousands of times larger than in the case of the Jovian moon Io, suggesting that large scale and intense volcanic activity can take place on TOI-179b. Its observability largely depends on the structure of its outer layers and the presence of an atmosphere, but this is an interesting candidate, and a good place to look for signs of volcanic plumes through transit observations.

6.5. Planet density: Comparison with other transiting planets

Aiming to put the high-density planet TOI-179 b in the context, we selected all planets with masses and radii measured with uncertainties better than 20% and 10%, respectively. We used the Exo-MerCat tool[9] (Alei et al. 2020) to retrieve the planetary parameters from the four main exoplanet archives[10] and produce the mass–radius (M–R) diagram in Fig. 15. The gray dots represent the known planet population, mainly composed of mature systems. We also add the young transiting exoplanets known to date (age <800 Myr) represented by the dots (color-coded according to age, see color bar on the right side of the plot). Because of the high level of stellar activity (hampering the recovery of the planetary signal) or because of the intrinsic difficulty to perform a proper RV follow-up (e.g., very faint stellar hosts), a robust determination of the planetary mass is not available for a significant fraction of the planets. These cases are depicted with colored triangles pointing toward lower values,

[9] User interface available at https://gitlab.com/eleonoraalei/exo-mercat-gui

[10] Exoplanets Encyclopaedia (http://exoplanet.eu/), the NASA Exoplanet Archive (https://exoplanetarchive.ipac.caltech.edu/), the Open Exoplanet Catalogue (https://www.openexoplanetcatalogue.com/), and The Exoplanet Data Explorer (http://exoplanets.org/)

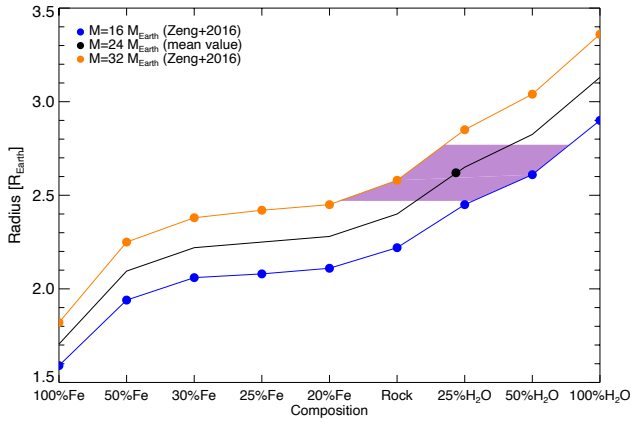

Fig. 16. Models of planetary composition reported from Zeng et al. (2016) for planets with 16 and 32 $M_\oplus$ (blue and orange curve, respectively). The black dot represents the putative location of TOI-179 b by considering a mean model between the considered models. The purple area indicates the range of compositions describing the structure of TOI-179 b.

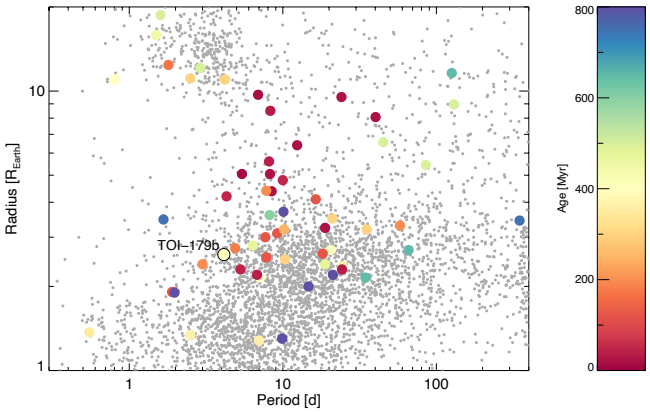

Fig. 17. Period–radius distribution of the transiting planets with radius known to better than 10% (gray dots). Planets younger than 800 Myr are depicted in different colors according to their age (see color bar).

since we only know the mass upper limits. Finally, the dashed lines indicate the location of equal planet density, as indicated at the top of the figure.

Figure 15 shows that TOI-179 b lies on the denser edge of the super-Earths–Neptune-like planets M–R distribution, at least among the planetary companions younger than ~800 Myr with measured mass. It has similar physical properties to Kepler-411 b, including a comparable orbital period of three days. The latter planet orbits a young (~200 Myr) K2V star with an external M-dwarf companion, which also denotes similarity between the stellar environments. On the other hand, Kepler-411 b belongs to a fairly compact four-planet system (Sun et al. 2019), indicating different formation and evolution paths. Among the well-characterized young and intermediate-age planets, K2-233 c also has a high density (see Fig. 15), placing it in the family of pure iron exoplanets (Lillo-Box et al. 2020). In addition, K2-233 c orbits a K3V star with age comparable to TOI-179, but (like Kepler-411) it belongs to a multi-planet system.

To investigate the possible composition of TOI-179 b, we considered Table 2 in Zeng et al. (2016) where models for planets with mass equal to 16 (blue curve in Fig. 16) and 32 $M_\oplus$ (orange curve) are reported. The curves describe the radius variation according to the possible planet composition. Since the measured mass for TOI-179 b is ~24 $M_\oplus$, we averaged the values reported by Zeng et al. (2016) to produce the model depicted with a black line and locate our target at the nominal value of the radius (black dot). Considering the error bars for both the mass and the radius, the planetary composition is described by the purple area in Fig. 16, ranging from pure rock with a small fraction of iron to 25% rock and 75% water, with typical structure showing 75% rock and 25% water.

Finally, Fig. 17 shows the period–radius diagram produced similarly to the M-R relation in Fig. 15. Even in this case, TOI-179 b is located at the edge of the typical distribution of super-Earths–Neptune-like planets. Unlike the case of very young planets (age $\lesssim$ 50 Myr, depicted as red dots), for which we expect a radius evolution with time leading to a shrinking of the planetary structure (see, e.g., the discussion in Benatti et al. 2021), TOI-179 b will probably remain in its current location of the diagram. As presented in Sect. 6.6, we do not foresee a significant loss of planetary atmosphere or the resulting reduction of radius (driven by the high-energy irradiation from the star) because of its high density.

6.6. Planet evaporation

In order to study the hydrodynamic stability of TOI-179 b, we applied our model described in Benatti et al. (2021) and Maggio et al. (2022), among others. In our model we describe the time evolution of planetary atmospheres of Neptunian planets using the hydrodynamic-based approach described in Kubyshkina et al. (2018) and adopting the evolution of the X-ray luminosity from Penz et al. (2008). Assuming that all the planetary mass is concentrated in the core, we found that the core radius is 2.33 $R_\oplus$, consequently, using the formula carried out by Lopez & Fortney (2014), we estimated the atmospheric mass fraction obtaining $f_{\rm atm}$ = 0.173%. This small value of $f_{\rm atm}$ suggests that the planet lost most of its primordial atmosphere. From the calculation of the Jeans parameter escape (e.g., Fossati et al. 2017), it results that the planet is stable against hydrodynamic evaporation, basically due to its high density.

We also investigated the past history of the planet to determine the past mass and radius values (at 10 Myr) for a planet that ends its evolution at the current stellar age with the observed mass and radius. We did not fix the core mass, but we explored a range of core masses, and at each of them we assigned different values of atmospheric mass fraction calculating consequently the initial planetary masses and radii. We have not been able to find a planet that ends its evolution with the mass and radius observed, other than the planet with the same mass and the same core mass previously estimated, but with a radius of 2.9 $R_\oplus$ that contracts down to the observed value only under the effect of the gravitational shrinking. This result is due to the fact that the most massive planets, which have larger radii even if they evaporate, cannot lose enough mass to reach the current observed value, while the less massive planets, due to the small corresponding radius, tend to rapidly become hydrodynamically stable, and therefore never reach the current mass (and radius) value.

7. Summary and perspectives

We presented the validation and characterization of the TOI-179 system. The central star is an active K2 star, with an age of 400±100 Myr determined by a variety of indicators and a

solar chemical composition. The star is orbited by a transiting planet with period 4.137436 days, mass $24\pm7\,M_{\oplus}$, radius $2.62^{+0.15}_{-0.12}\,R_{\oplus}$, and significant eccentricity ($0.34^{+0.07}_{-0.09}$), identified as a planet candidate by TESS and confirmed by extended RV time series obtained with HARPS. AO observations with SPHERE identified a low-mass companion at the boundary between brown dwarfs and very low-mass stars (mass from luminosity $83^{+4}_{-6}M_{\rm J}$) at a very small projected separation (84.5 mas, 3.3 au at the distance of the star). Coupling the imaging detection with the long-term RV trend and the astrometric signature (proper motion anomaly considering HIPPARCOS and *Gaia* data), we constrained the orbit of the low-mass companion, identifying two families of possible orbital solutions, one with shorter period (∼20–40 yr) and very high eccentricity (∼0.9) and the other with longer period (∼100–120 yr) and moderate eccentricity (∼0.3–0.5). The closest family of orbital solutions would imply strong dynamical interactions with the transiting planet. The architecture of the system is completed by a close pair (separation about 1″) of K dwarfs at a projected separation of 3400 au from TOI-179.

The system is suitable for several follow-up observations. First of all, the incomplete orbit coverage of the outer low-mass companion calls for further observations both in imaging and radial velocity to firmly determine the orbital solution and the dynamical mass of the object. Future *Gaia* releases will also provide relevant contributions. In the near future, with a larger projected separation from the central star, spectroscopic observations of the companion will also become feasible, increasing the role of HD 18599 B as a benchmark low-mass object.

The determination of the orbit of the outer companion will allow us to understand its influence on the orbital parameters of the transiting planet, necessary to understand the origin of its eccentricity. The dynamical link between the two objects can also be investigated through transit time variations (TTVs).

The measure of the planetary orbital obliquity with respect to the stellar spin axis could be relevant to place further constraints on the system architecture and its evolution with time. This issue can be investigated through the measurement of the Rossiter–McLaughlin (RM) effect: the expected RM amplitude is $\sim3.6\,{\rm m\,s^{-1}}$ (by using Eq. (40) in Winn 2010), potentially detectable with ESPRESSO at VLT.

Further spectroscopic and photometric observations will also allow us to reduce the uncertainties on planet parameters and then to better infer its evolutionary path (e.g., evaporation). Finally, the planet is also a possible target for atmospheric characterization, although its compact structure and high density do not give it a particularly high rank for this aim among planets of similar radii (a value of 52 is derived for the metric of transmission spectrum proposed by Kempton et al. 2018). The possibility of the occurrence of intense volcanic activity is of special interest in this context. In brief, the system of TOI-179 presented in this paper is a potential high-merit laboratory for our understanding of the physical evolution of planets and other low-mass objects and of how the planet properties are influenced by dynamical effects and interactions with the parent star.

Acknowledgements. We acknowledge the use of public TESS Alert data from pipelines at the TESS Science Office and at the TESS Science Processing Operations Center. Funding for the TESS mission is provided by NASA's Science Mission directorate. This work has made use of data from the European Space Agency (ESA) mission *Gaia* (https://www.cosmos.esa.int/gaia), processed by the *Gaia* Data Processing and Analysis Consortium (DPAC, https://www.cosmos.esa.int/web/gaia/dpac/consortium). Funding for the DPAC has been provided by national institutions, in particular the institutions participating in the *Gaia* Multilateral Agreement. This work has made use of the SPHERE Data Centre, jointly operated by OSUG/IPAG (Grenoble), PYTHEAS/LAM/CeSAM (Marseille), OCA/Lagrange (Nice), Observatoire de Paris/LESIA (Paris), and Observatoire de Lyon/CRAL, and supported by a grant from Labex OSUG@2020 (Investissements d'avenir – ANR10 LABX56). We thank F. Bouchy and X. Dumusque for managing the sharing of observing time between several programmes approved for HARPS in P103 and the observers of these programmes for carrying out observations of our target in their nights. This work has been supported by the PRIN-INAF 2019 "Planetary systems at young ages (PLATEA)" and ASI-INAF agreement no. 2018-16-HH.0. D.L. acknowledges the support from ASI-INAF agreement no. 2021-5-HH.0. D.N. acknowledges the support from the French Centre National d'Etudes Spatiales (CNES). A.S. acknowledges support from the Italian Space Agency (ASI) under contract 2018-24-HH.0 "The Italian participation to the *Gaia* Data Processing and Analysis Consortium (DPAC)" in collaboration with the Italian National Institute of Astrophysics. The authors became aware of a parallel effort on the characterization of TOI-179 by Vines et al. (2022) in the late stages of the manuscript preparations. Only submissions to arxiv were coordinated, and no analyses or results were shared prior to the acceptance of the papers.

References

Alei, E., Claudi, R., Bignamini, A., & Molinaro, M. 2020, Astron. Comput., 31, 100370
Allard, F., Guillot, T., Ludwig, H.-G., et al. 2003, in IAU Symposium, 211, 325
Ambikasaran, S., Foreman-Mackey, D., Greengard, L., Hogg, D. W., & O'Neil, M. 2015, IEEE Trans. Pattern Anal. Mach. Intell., 38
Ammler-von Eiff, M., & Guenther, E. W. 2009, A&A, 508, 677
Anglada-Escudé, G., & Butler, R. P. 2012, ApJS, 200, 15
Bailer-Jones, C. A. L., Rybizki, J., Fouesneau, M., Demleitner, M., & Andrae, R. 2021, AJ, 161, 147
Baliunas, S. L., Donahue, R. A., Soon, W. H., et al. 1995, ApJ, 438, 269
Baraffe, I., Homeier, D., Allard, F., & Chabrier, G. 2015, A&A, 577, A42
Barnes, J. R., Haswell, C. A., Staab, D., et al. 2020, Nat. Astron., 4, 419
Barragán, O., Armstrong, D. J., Gandolfi, D., et al. 2022, MNRAS, 514, 1606
Benatti, S., Nardiello, D., Malavolta, L., et al. 2019, A&A, 630, A81
Benatti, S., Damasso, M., Borsa, F., et al. 2021, A&A, 650, A66
Beuzit, J. L., Vigan, A., Mouillet, D., et al. 2019, A&A, 631, A155
Biazzo, K., Gratton, R., Desidera, S., et al. 2015, A&A, 583, A135
Biazzo, K., D'Orazi, V., Desidera, S., et al. 2022, A&A, 664, A161
Bonavita, M., Fontanive, C., Gratton, R., et al. 2022a, MNRAS, 513, 5588
Bonavita, M., Gratton, R., Desidera, S., et al. 2022b, A&A, 663, A144
Bonnell, I. A., Smith, K. W., Davies, M. B., & Horne, K. 2001, MNRAS, 322, 859
Bouma, L. G., Hartman, J. D., Brahm, R., et al. 2020, AJ, 160, 239
Brandt, T. D., Dupuy, T. J., Bowler, B. P., et al. 2020, AJ, 160, 196
Bryan, M. L., Knutson, H. A., Lee, E. J., et al. 2019, AJ, 157, 52
Bryson, S., Kunimoto, M., Kopparapu, R. K., et al. 2021, AJ, 161, 36
Buchner, J., Georgakakis, A., Nandra, K., et al. 2014, A&A, 564, A125
Canto Martins, B. L., Gomes, R. L., Messias, Y. S., et al. 2020, ApJS, 250, 20
Carleo, I., Malavolta, L., Lanza, A. F., et al. 2020, A&A, 638, A5
Carleo, I., Desidera, S., Nardiello, D., et al. 2021, A&A, 645, A71
Carolo, E., Desidera, S., Gratton, R., et al. 2014, A&A, 567, A48
Castelli, F., & Kurucz, R. L. 2003, in IAU Symposium, 210, A20
Chauvin, G. 2018, SPIE Conf. Ser., 10703, 1070305
Chauvin, G., Lagrange, A. M., Udry, S., et al. 2006, A&A, 456, 1165
Ciardi, D. R., Crossfield, I. J. M., Feinstein, A. D., et al. 2018, AJ, 155, 10
Claudi, R. U., Turatto, M., Gratton, R. G., et al. 2008, SPIE Conf. Ser., 7014, 70143E
Correia, A. C. M., Bourrier, V., & Delisle, J. B. 2020, A&A, 635, A37
da Silva, L., Girardi, L., Pasquini, L., et al. 2006, A&A, 458, 609
Damasso, M., Lanza, A. F., Benatti, S., et al. 2020, A&A, 642, A133
David, T. J., Petigura, E. A., Luger, R., et al. 2019, ApJ, 885, L12
Delorme, P., Meunier, N., Albert, D., et al. 2017, in SF2A-2017: Proceedings of the Annual meeting of the French Society of Astronomy and Astrophysics, eds. C. Reylé, P. Di Matteo, & F. Herpin
Desidera, S., Covino, E., Messina, S., et al. 2015, A&A, 573, A126
Desidera, S., Chauvin, G., Bonavita, M., et al. 2021, A&A, 651, A70
Dohlen, K., Langlois, M., Saisse, M., et al. 2008, SPIE Conf. Ser., 7014, 70143L
D'Orazi, V., Oliva, E., Bragaglia, A., et al. 2020, A&A, 633, A38
Drimmel, R., Sozzetti, A., Schröder, K.-P., et al. 2021, MNRAS, 502, 328
Eastman, J., Gaudi, B. S., & Agol, E. 2013, PASP, 125, 83
Engler, N., Lazzoni, C., Gratton, R., et al. 2020, A&A, 635, A19
Fabricius, C., Høg, E., Makarov, V. V., et al. 2002, A&A, 384, 180
Feng, F., Butler, R. P., Shectman, S. A., et al. 2020, ApJS, 246, 11
Feroz, F., Hobson, M. P., Cameron, E., & Pettitt, A. N. 2019, Open J. Astrophys., 2, 10
Fontanive, C., Rice, K., Bonavita, M., et al. 2019, MNRAS, 485, 4967
Ford, E. B. 2006, ApJ, 642, 505

Fossati, L., Erkaev, N. V., Lammer, H., et al. 2017, A&A, 598, A90
Gagné, J., Mamajek, E. E., Malo, L., et al. 2018, ApJ, 856, 23
Gaia Collaboration (Smart, R. L., et al.) 2021, A&A, 649, A6
Galicher, R., Boccaletti, A., Mesa, D., et al. 2018, A&A, 615, A92
Gomes da Silva, J., Figueira, P., Santos, N., & Faria, J. 2018, J. Open Source Softw., 3, 667
Gondoin, P. 2014, A&A, 566, A72
Grandjean, A., Lagrange, A. M., Keppler, M., et al. 2020, A&A, 633, A44
Grandjean, A., Lagrange, A. M., Meunier, N., et al. 2021, A&A, 650, A39
Gray, R. O., Corbally, C. J., Garrison, R. F., et al. 2006, AJ, 132, 161
Haywood, R. D., Collier Cameron, A., Queloz, D., et al. 2014, MNRAS, 443, 2517
Hippke, M., & Heller, R. 2019, A&A, 623, A39
Hirsch, L. A., Ciardi, D. R., Howard, A. W., et al. 2017, AJ, 153, 117
Horch, E. P., Howell, S. B., Everett, M. E., & Ciardi, D. R. 2014, ApJ, 795, 60
Howard, A. W., Marcy, G. W., Bryson, S. T., et al. 2012, ApJS, 201, 15
Howard, W. S., Teske, J., Corbett, H., et al. 2021, AJ, 162, 147
Huang, C. X., Vanderburg, A., Pál, A., et al. 2020, RNAAS, 4, 204
Jenkins, J. M., Twicken, J. D., McCauliff, S., et al. 2016, SPIE Conf. Ser., 9913, 99133E
Jenkins, J. S., Jones, H. R. A., Pavlenko, Y., et al. 2008, A&A, 485, 571
Jenkins, J. S., Murgas, F., Rojo, P., et al. 2011, A&A, 531, A8
Jones, B. F., Fischer, D., Shetrone, M., & Soderblom, D. R. 1997, AJ, 114, 352
Kaib, N. A., Raymond, S. N., & Duncan, M. 2013, Nature, 493, 381
Kempton, E. M. R., Bean, J. L., Louie, D. R., et al. 2018, PASP, 130, 114401
Kervella, P., Arenou, F., & Thévenin, F. 2022, A&A, 657, A7
Klein, B., Donati, J.-F., Moutou, C., et al. 2021, MNRAS, 502, 188
Kreidberg, L. 2015, PASP, 127, 1161
Kubyshkina, D., Fossati, L., Erkaev, N. V., et al. 2018, A&A, 619, A151
Lanza, A. F. 2021, A&A, 653, A112
Leconte, J., Chabrier, G., Baraffe, I., & Levrard, B. 2010, A&A, 516, A64
Lillo-Box, J., Lopez, T. A., Santerne, A., et al. 2020, A&A, 640, A48
Lin, D. N. C., Bodenheimer, P., & Richardson, D. C. 1996, Nature, 380, 606
Lind, K., Asplund, M., Barklem, P. S., & Belyaev, A. K. 2011, A&A, 528, A103
Linder, E. F., Mordasini, C., Mollière, P., et al. 2019, A&A, 623, A85
Lo Curto, G., Pepe, F., Avila, G., et al. 2015, The Messenger, 162, 9
Lopez, E. D., & Fortney, J. J. 2014, ApJ, 792, 1
Lovis, C., Dumusque, X., Santos, N. C., et al. 2011, arXiv e-prints [arXiv:1107.5325]
Maggio, A., Locci, D., Pillitteri, I., et al. 2022, ApJ, 925, 172
Mamajek, E. E., & Hillenbrand, L. A. 2008, ApJ, 687, 1264
Mann, A. W., Vanderburg, A., Rizzuto, A. C., et al. 2018, AJ, 155, 4
Mann, A. W., Johnson, M. C., Vanderburg, A., et al. 2020, AJ, 160, 179
Marois, C., Correia, C., Galicher, R., et al. 2014, SPIE Conf. Ser., 9148, 91480U
Marzari, F., & Barbieri, M. 2007, A&A, 467, 347
Mason, B. D., Wycoff, G. L., Hartkopf, W. I., Douglass, G. G., & Worley, C. E. 2001, AJ, 122, 3466
Mawet, D., Milli, J., Wahhaj, Z., et al. 2014, ApJ, 792, 97
Mayor, M., Pepe, F., Queloz, D., et al. 2003, The Messenger, 114, 20
Mesa, D., Gratton, R., Zurlo, A., et al. 2015, A&A, 576, A121
Messina, S., Nardiello, D., Desidera, S., et al. 2022, A&A, 657, L3
Miller, N., Fortney, J. J., & Jackson, B. 2009, ApJ, 702, 1413
Montalto, M., Piotto, G., Marrese, P. M., et al. 2021, A&A, 653, A98
Montes, D., López-Santiago, J., Gálvez, M. C., et al. 2001, MNRAS, 328, 45
Mordasini, C., Alibert, Y., Klahr, H., & Henning, T. 2012, A&A, 547, A111
Mortier, A., Santos, N. C., Sousa, S., et al. 2013, A&A, 551, A112
Mugrauer, M., & Michel, K.-U. 2020, Astron. Nachr., 341, 996
Nakajima, T., Oppenheimer, B. R., Kulkarni, S. R., et al. 1995, Nature, 378, 463
Nardiello, D. 2020, MNRAS, 498, 5972
Nardiello, D., Bedin, L. R., Nascimbeni, V., et al. 2015, MNRAS, 447, 3536
Nardiello, D., Libralato, M., Bedin, L. R., et al. 2016, MNRAS, 455, 2337
Nardiello, D., Borsato, L., Piotto, G., et al. 2019, MNRAS, 490, 3806
Nardiello, D., Piotto, G., Deleuil, M., et al. 2020, MNRAS, 495, 4924
Nardiello, D., Malavolta, L., Desidera, S., et al. 2022, A&A, 664, A163
Newton, E. R., Mann, A. W., Tofflemire, B. M., et al. 2019, ApJ, 880, L17
Newton, E. R., Mann, A. W., Kraus, A. L., et al. 2021, AJ, 161, 65
Nielsen, E. L., Rosa, R. J. D., Rameau, J., et al. 2017, AJ, 154, 218
Noyes, R. W., Hartmann, L. W., Baliunas, S. L., Duncan, D. K., & Vaughan, A. H. 1984, ApJ, 279, 763
Oelkers, R. J., Rodriguez, J. E., Stassun, K. G., et al. 2018, AJ, 155, 39
Ogilvie, G. I. 2014, ARA&A, 52, 171
Pavlov, A., Möller-Nilsson, O., Feldt, M., et al. 2008, SPIE Conf. Ser., 7019, 701939
Pecaut, M. J., & Mamajek, E. E. 2013, ApJS, 208, 9
Penz, T., Micela, G., & Lammer, H. 2008, A&A, 477, 309
Pinamonti, M., Sozzetti, A., Maldonado, J., et al. 2022, A&A, 664, A65
Plavchan, P., Barclay, T., Gagné, J., et al. 2020, Nature, 582, 497
Pojmanski, G. 1997, Acta Astron., 47, 467
Rasio, F. A., Tout, C. A., Lubow, S. H., & Livio, M. 1996, ApJ, 470, 1187
Rebull, L. M., Stauffer, J. R., Bouvier, J., et al. 2016, AJ, 152, 114
Rebull, L. M., Stauffer, J. R., Hillenbrand, L. A., et al. 2017, ApJ, 839, 92
Ricker, G. R., Winn, J. N., Vanderspek, R., et al. 2015, J. Astron. Telescopes Instrum. Syst., 1, 014003
Rizzuto, A. C., Mann, A. W., Vanderburg, A., Kraus, A. L., & Covey, K. R. 2017, AJ, 154, 224
Rizzuto, A. C., Newton, E. R., Mann, A. W., et al. 2020, AJ, 160, 33
Schwarz, R., Funk, B., Zechner, R., & Bazsó, Á. 2016, MNRAS, 460, 3598
Smith, J. C., Stumpe, M. C., Van Cleve, J. E., et al. 2012, PASP, 124, 1000
Sneden, C. A. 1973, PhD thesis, The University of Texas at Austin, USA
Soderblom, D. R., Pilachowski, C. A., Fedele, S. B., & Jones, B. F. 1993, AJ, 105, 2299
Soummer, R., Pueyo, L., & Larkin, J. 2012, ApJ, 755, L28
Sousa, S. G., Santos, N. C., Israelian, G., Mayor, M., & Monteiro, M. J. P. F. G. 2007, A&A, 469, 783
Stamatellos, D., & Whitworth, A. P. 2009, MNRAS, 392, 413
Stassun, K. G., Oelkers, R. J., Paegert, M., et al. 2019, AJ, 158, 138
Stumpe, M. C., Smith, J. C., Van Cleve, J. E., et al. 2012, PASP, 124, 985
Stumpe, M. C., Smith, J. C., Catanzarite, J. H., et al. 2014, PASP, 126, 100
Suárez Mascareño, A., Damasso, M., Lodieu, N., et al. 2021, Nat. Astron., 6, 232
Sun, L., Ioannidis, P., Gu, S., et al. 2019, A&A, 624, A15
Ter Braak, C. J. F. 2006, Stat. Comput., 16, 239
Thebault, P., & Haghighipour, N. 2015, in Planetary Exploration and Science: Recent Results and Advances, 309
Tobie, G., Grasset, O., Dumoulin, C., & Mocquet, A. 2019, A&A, 630, A70
Tokovinin, A. 2016, ApJ, 831, 151
Tokovinin, A., & Lépine, S. 2012, AJ, 144, 102
Torres, G., Konacki, M., Sasselov, D. D., & Jha, S. 2004, ApJ, 614, 979
Tuomi, M., Jones, H. R. A., Barnes, J. R., Anglada-Escudé, G., & Jenkins, J. S. 2014, MNRAS, 441, 1545
Veras, D., Crepp, J. R., & Ford, E. B. 2009, ApJ, 696, 1600
Vigan, A., Moutou, C., Langlois, M., et al. 2010, MNRAS, 407, 71
Vines, J. I., Jenkins, J. S., Berdiñas, Z., et al. 2022, MNRAS
Weidenschilling, S. J., & Marzari, F. 1996, Nature, 384, 619
Winn, J. N. 2010, arXiv e-prints [arXiv:1001.2010]
Wu, Y., Murray, N. W., & Ramsahai, J. M. 2007, ApJ, 670, 820
Zechmeister, M., Kürster, M., & Endl, M. 2009, A&A, 505, 859
Zeng, L., Sasselov, D. D., & Jacobsen, S. B. 2016, ApJ, 819, 127
Zhou, G., Quinn, S. N., Irwin, J., et al. 2021, AJ, 161, 2
Zicher, N., Barragán, O., Klein, B., et al. 2022, MNRAS, 512, 3060
Ziegler, C., Tokovinin, A., Briceño, C., et al. 2020, AJ, 159, 19
Zurlo, A., Vigan, A., Mesa, D., et al. 2014, A&A, 572, A85

Appendix A: Stellar parameters

We present in this Appendix the details of the determination of the stellar parameters for TOI-179 and its wide companions, CD-56 593 A and B, briefly summarized in Sect. 3.

Appendix A.1: Spectroscopic analysis

We exploited the HARPS spectra described in Sect. 2.2 for the stellar characterization. A co-added spectrum was created, The composite spectrum has S/N per pixel at 6700 Å of 180.

Our aim was to derive the spectroscopic parameters and metallicity ([Fe/H]) via the equivalent width (EW) method and the standard iron line analysis. EWs were measured using *ARES* (Sousa et al. 2007), with frequent visual inspection and manual re-adjustment using the *IRAF* task *splot* (performing Gaussian fits). We adopted the linelist by D'Orazi et al. (2020), which includes 80 Fe I and 17 Fe II lines (see that paper for details on atomic parameters). We used the Castelli & Kurucz grid of model atmosphere, with new opacities and no overshooting (ODFNEW, Castelli & Kurucz 2003). Stellar parameters ($T_{\rm eff}$, log g, microturbulence velocity Vt) and metallicity were derived in a semi-automated way using the MOOG (Sneden 1973) python wrapper qoyllur-quipu (q^2) code developed by I. Ramírez[11]. We first derived the parameters and metallicity for the HARPS-N solar spectrum obtained by Biazzo et al. (2022) and found $T_{\rm eff}$=5790±43 K, log $g_{\odot}$=4.44±0.10 dex, Vt=0.97±0.07 km s^{-1}, and log n(Fe I)= 7.49±0.03 dex. The internal uncertainties reported on atmospheric parameters come from errors on the slopes for $T_{\rm eff}$ and Vt, whereas those on surface gravity come from errors on the ionization balance condition of iron, as also routinely done in our previous works (Biazzo et al. 2015; D'Orazi et al. 2020, and references therein).

We found $T_{\rm eff}$=5172±60 K, logg=4.54±0.09 dex, Vt=1.09±0.14 kms^{-1}, and [Fe/H]=0.00±0.08 dex (total error). Previously, Mortier et al. (2013) reported $T_{\rm eff}$=5154 K (from B-V color) and [Fe/H]=-0.01 dex (from their calibration of CCF parameters), while Jenkins et al. (2008) derived [Fe/H]=-0.01 dex (from their analysis of FEROS spectra; $T_{\rm eff}$ not listed). A comparison with the photometric sequences by Pecaut & Mamajek (2013) [12] yields a photometric $T_{\rm eff}$=5118±50 K, assuming no reddening as the target is at only 38 pc from the Sun. Independent measurements then agree fairly well. In the following we adopt the mean of our spectroscopic and photometric determinations, $T_{\rm eff}$=5145 K, with a conservative error of 50 K.

Appendix A.2: Chemical abundances

We determined the elemental abundances for proton-capture, α, and iron-peak elements Na I, Mg I, Al I, Ca I, Ti I, Ti II, and Ni I by using the line list of D'Orazi et al. (2020) and the same code and model atmosphere described in Sect. A.1. As previously done for the [Fe/H] determination, we first analysed the solar spectrum and obtained the elemental abundances reported in Table A.1. For the Na I lines 6154/6160 Å we applied non-local termodynamic equlibrium (NLTE) corrections from the INSPECT database (Lind et al. 2011). We calculated internal errors due to EW measurements (the first error in Table A.1, which is the error on the mean from different lines) and the uncertainty related to atmospheric parameters. All the abundances exhibit a solar-scaled pattern, with only a marginal enhancement in calcium ([Ca/H]=0.07 dex) and titanium ([Ti/H]=0.07 from the average of neutral and singly-ionized atomic lines). This is probably related to blending effects of the lines and/or continuum displacements at lower temperatures.

Species	N-lines	Sun	TOI-179
Na I$_{\rm NLTE}$	2	6.21±0.01±0.01	6.21±0.01±0.02
Mg I	2	7.56±0.03±0.01	7.59±0.03±0.02
Al I	2	6.51±0.01±0.01	6.56±0.01±0.01
Si I	11	7.49±0.02±0.02	7.47±0.01±0.02
Ca I	9	6.32±0.04±0.01	6.39±0.03±0.01
Ti I	52	4.96±0.04±0.02	5.05±0.04±0.03
Ti II	25	4.97±0.05±0.02	5.03±0.06±0.04
Ni I	16	6.24±0.01±0.02	6.24±0.02±0.03

Table A.1: Elemental abundances (with corresponging number of lines) as derived for the solar spectrum and TOI-179.

Appendix A.3: Lithium

We also exploited the HARPS spectrum to measure the equivalent width (EW) of the Li 6708Å doublet, which results in a value of 39.3±4.5 mÅ. The Li EW of TOI-179 is between those of the Pleiades and Hyades of similar colors (Fig. A.1), close but slightly smaller than that of M34 members (Jones et al. 1997; Gondoin 2014), and close to the upper envelope of the members of Ursa Major moving group (Soderblom et al. 1993; Ammler-von Eiff & Guenther 2009).

We employed the stellar parameters derived in Section A.1 and performed spectral synthesis calculations in order to derive the Li abundance. We used the driver *synth* in MOOG (2019 version) and the line list around the Li doublet at 6708Å, as was done in our previous investigations. By adopting a FWHM of 0.06 Å for the instrumental profile and a limb darkening of 0.65, we determined A(Li I)=1.55±0.08 dex (see Fig. A.2).

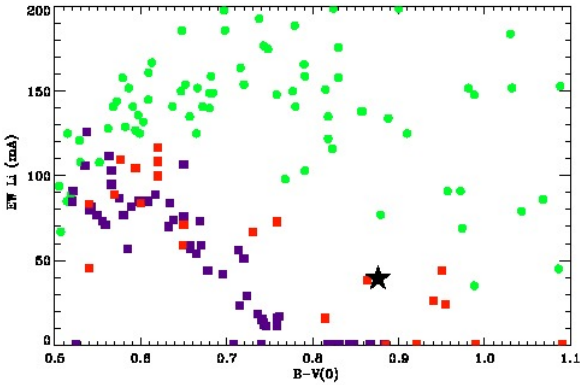

Fig. A.1: Equivalent width for Li of TOI-179 (black star) compared to those of the members of the Pleiades (green circles), Hyades (purple squares), and Ursa Major (red squares).

[11] The code and the tutorial are available at https://github.com/astroChasqui/q2.
[12] Updated version available at https://www.pas.rochester.edu/~emamajek/EEM_dwarf_UBVIJHK_colors_Teff.txt, hereafter referred to as Mamajek tables

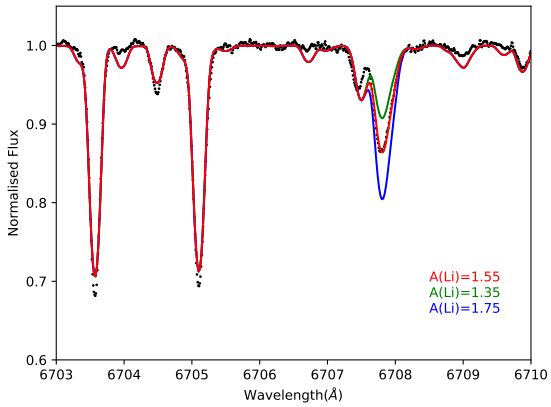

Fig. A.2: Comparison between observed (black dots) and synthetic (green, red, and blue lines) spectra around the Li I line at 6708 Å.

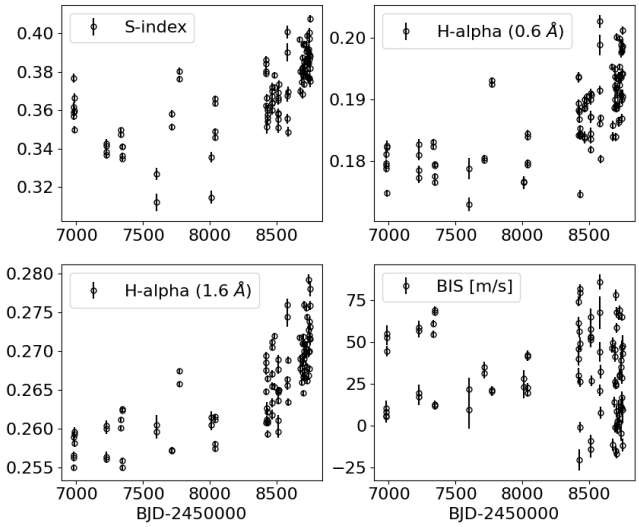

Fig. A.3: Time series of Ca II H&K instrumental S index, Hα, and bisector velocity span (BIS).

Appendix A.4: Projected rotational velocity

We derived the projected rotational velocity $v \sin i$ exploiting the HARPS spectra with two independent methods. From the spectral synthesis in the region of the Li doublet, we derived $v \sin i$ = 4.5 ± 0.5 km s^{-1}. From a preliminary calibration of the observed FWHM of the CCF into rotational velocity for HARPS spectra, we obtained $v \sin i$ = 4.50 ± 0.41 km s^{-1}. Determinations available in the literature are 4.3 km s^{-1} (Jenkins et al. 2011) and 4.6 km s^{-1} (Grandjean et al. 2021), in good agreement with our determinations.

Appendix A.5: Chromospheric and coronal activity

We measured the instrumental S index (Ca II H&K) and Hα index using the tool ACTIN (v1.3.9; Gomes da Silva et al. 2018). We calculated the Hα index adopting both the definitions labeled "Ha06" and "Ha16" in the line configuration file, denoting indices with 0.6 and 1.6 Å central bandwidths, respectively. The most relevant signal is a long-term modulation, likely ascribed to an activity cycle, which is nearly linear in Hα (especially for the case of the Ha16 index), while a possible turnover is observed for the S index (Fig. A.3). This difference may be real, and linked to the different kinds of active regions to which each indicator is sensitive, but might also be due to the modification of the HARPS setup in 2015 (Lo Curto et al. 2015). A nearly linear upward trend is also seen in the RV time series (see Sect. 4.3). Dedicated tests were performed and presented in Sect. 5.1 supporting the Keplerian origin of the RV trend.

After removing the long-term trend, a significant periodicity at 8.64 d appears on the residuals of the S index time series, corresponding to the rotation period of the star, while no significant short-term periodicity is found for Hα.

As the ACTIN S index is not calibrated into the standard Mount Wilson scale (Baliunas et al. 1995), we also obtained calibrated S_{MW} index using the procedure adopted in Desidera et al. (2015). The mean values result in S_{MW}=0.607 and, with B-V color from Table 2 and Noyes et al. (1984) transformation, in $\log R'_{HK}$=-4.35. The minimum and maximum values considering the prominent long-term activity cycle are $\log R'_{HK}$=-4.43 and -4.30, respectively. The sparse measurements by Gray et al. (2006), Jenkins et al. (2008), and Jenkins et al. (2011) are within this distribution. The activity level is intermediate between Hyades and Pleiades/AB Dor stars of similar colors.

From the CHANDRA observations described in Sect. 2.4, we obtained for TOI-179 a kT of 0.56 keV and an unabsorbed flux of 1.79×10^{-13} erg s^{-1} cm^{-2} in the ROSAT band 0.1–2.4 keV which corresponds to a X-ray luminosity of $L_X \approx 3.23 \times 10^{28}$ erg s^{-1} at a distance of 38.6 pc. The normalization constant of the best-fit model corresponds to an emission measure of 2.7×10^{51} cm^{-3}. Coupled with the stellar luminosity from Table 2, this implies $R_X = \log(L_X/L_{\rm bol}) = -4.65$, slighty above the median value of Hyades members of similar colors.

Appendix A.6: Photometric variability and rotation period

Three determinations of rotation period of TOI-179 are available in the literature. Oelkers et al. (2018) measured a period of 8.693d from KELT photometric data, Howard et al. (2021) obtained P=8.64±0.04 d from their analysis of TESS and Evryscope data, and Canto Martins et al. (2020) derived P=8.49±0.86 d considering TESS data only (sectors 2–3). Our analysis of TESS light curves (four sectors considered independently) performed with the methods described in Messina et al. (2022) yields a photometric period of 8.84±0.29 d (see Fig. A.4), in general agreement with the literature results. The analysis of the time series of HARPS RV and the corresponding activity indicators also provides additional estimates of rotation periods. The Gaussian process regression analysis of the RV time series described in Sect. 4.3 yields a period of 8.72±0.04 d, while the S index periodogram analysis (Sect. A.5) indicates a period of 8.64 d. Averaging the above determinations, we derive P= 8.73±0.07 d.

The adopted rotation period is slightly longer than the rotation-color sequence of the 300 Myr Group X recently obtained by Messina et al. (2022). It is clearly distinct from the Pleiades sequence on the young side and from Hyades and Praesepe on the old side (Fig. A.5). From the Mamajek & Hillenbrand (2008) calibration, the resulting age is 390 Myr.

Finally, to further constrain the long-term activity variations we also checked the ASAS light curve (Pojmanski 1997), which covers about 9 yr between 2000 and 2009. A small downward trend of 0.003±0.0003 mag yr^{-1} is retrieved, without indications of large long-term photometric variations and significant periodicities due to an activity cycle.

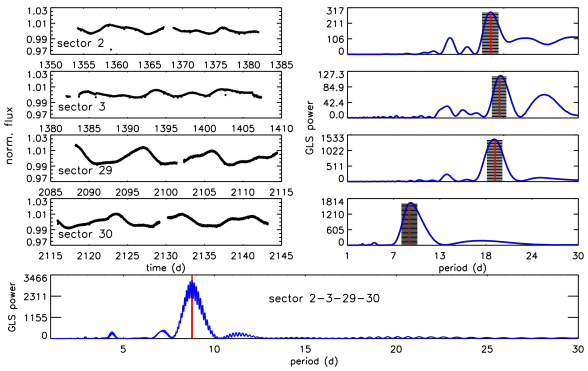

Fig. A.4: TESS light curves in Sectors 2, 3, 29, and 30 (from top to bottom) represented as normalized flux vs. time (left column), and corresponding GLS periodograms (right column) with indication of the measured periodicity (vertical red line) and its uncertainty (shaded region). Similar periodograms are obtained when using CLEAN (see Messina et al. 2022). The bottom plot shows the periodogram when all four sectors are combined into a unique time series.

Appendix A.7: Kinematics and membership to groups

TOI-179 is not a member of known moving groups according to our analysis using the BANYAN Σ code by Gagné et al. (2018) [13]. Nevertheless, its kinematic parameters are well within the kinematic box of young stars (Montes et al. 2001). A full-sky search in the Gaia Collaboration et al. (2021) catalog for stars with similar space velocity components U,V,W with parallax larger than 15 mas yields only 13 stars with a difference in each of the space velocities of less than 2 km s^{-1} with respect to TOI-179[14]. These stars are scattered over the whole sky; only some of them give an indication of being moderately active and young, but likely older than TOI-179; the majority give no indication of youth except for the kinematics, and one is clearly an older a red giant. We conclude that our target is not part of any group or association.

Appendix A.8: Multiplicity: The wide companions CD-56 593 A and B

TOI-179 is a known triple system. CD-56 593 is a close pair (1.50" = 58 au projected separation at the date of the first observation listed in WDS (Mason et al. 2001), epoch 1911; 1.20"= 46 au projected separation in 1991 (Fabricius et al. 2002); $\Delta V = 0.76$ mag) at 87.5" almost exactly south (PA = 182 degree) from TOI-179, corresponding to a physical projected separation of 3380 au. The close binary is not resolved in Gaia DR2, while there are separate entries in Gaia EDR3, with a projected separation of 0.90", a significant position angle shift (194 deg, compared to 185 deg in 1911), and a magnitude difference ΔG=0.55 mag. The differences in the proper motion between the components and with respect to TOI-179 are linked to orbital motion and they are small enough to firmly conclude on the physical association with TOI-179. The common proper motion was previously noted by Tokovinin & Lépine (2012) and Mugrauer & Michel (2020). No other comoving objects are found in Gaia EDR3 within 1 deg. The presence of close companions are discussed in Sect. 5.

[13] http://www.exoplanetes.umontreal.ca/banyan/banyansigma.php

[14] The wide companion CD-56 593 (see Sect. A.8) is not included in this output because it lacks radial velocity determinations

The position of the components on the M_G versus $BP - RP$ color–magnitude diagram agrees within the errors with the standard main sequence in the Mamajek tables. The expected spectral types are K5 and K6/K7 (closer to K7) for CD-56 593A and CD-56 593B, respectively, and the stellar masses 0.70 and 0.66 M$_\odot$ for CD-56 593A and CD-56 593B, respectively. The system is thus formed by three K dwarfs.

CD-56 593 has a photometric rotation period (which most likely belongs to the brighter component CD-56 593A) of 11.20 d (Oelkers et al. 2018). We also analyzed the TESS data as was done for TOI-179 in Sect. A.6. We found a period similar to the literature value for the Sector 2 data, while a period close to a half of this value was derived for the Sector 30 data, most likely a harmonic of the true period linked to the distribution of starspots on stellar surface. The period in Sector 29 is instead uncertain as it appears dominated by the evolution of active regions or variable contributions from the two components. The data in Sector 3 are of poor quality. Combining the data, we adopt a period of 11.2±0.9 d. After deblending of the Ks magnitude following the Mamajek tables, this period is slightly slower than the sequence of the 300 Myr old Group X, as found above for TOI-179, independently of the component to which the observed periodicity belongs to (Fig. A.5).

CD-56 583 is also detected in the CHANDRA images presented in Sect. 2.4, with spatially unresolved emission between the two components. We obtained a temperature of 0.67 keV and an unabsorbed flux of 1.13×10^{-13} erg s^{-1} cm^{-2} in the ROSAT band, corresponding to a system X-ray luminosity of 2.03×10^{28} erg/s. We also obtained a value of emission measure for each component equal to $\sim 8 \times 10^{50}$ cm^{-3}. An estimated value of the X-ray luminosities of the individual components, assuming they have the same R_X ratio (R_X=-4.74, from the individual luminosities of 0.181 and 0.112 L$_\odot$, for CD-56 593A and CD-56 593B, respectively, derived as in Sect. A.10), is 1.25×10^{28} erg/s and 0.78×10^{28} erg/s for CD-56 593A and CD-56 593B, respectively. These values are similar to those of Hyades members of similar spectral type.

Appendix A.9: Age

The age indicators of TOI-179 consistently support an age older than the Pleiades and younger than the Hyades. A comparison with the 300 Myr old Group X moving group indicates a slighty older age. Isochrone fitting supports an age close to the main sequence, consistently with the indirect age indicators, both for TOI-179 and for CD-56 593 A and B (within the large color uncertainties for these latter objects). Considering these results, we rely on indirect indicators, of which the most sensitive (given the age and spectral type of the object) are the lithium and rotation period. We adopt an age of 400 Myr with limits between 300 to 500 Myr. The results of the wide binary companion CD-56 593 (CMD position, rotation period, and X-ray emission) are also consistent with this age estimate.

Appendix A.10: Mass, radius, and system orientation

We exploited the PARAM web interface (da Silva et al. 2006)[15] to infer the stellar mass. As in Desidera et al. (2015), we restricted the values of stellar ages to those allowed by indirect methods. This shifts the stellar mass upward by about 0.03 M$_\odot$. The final adopted mass is 0.863±0.020 M$_\odot$.

[15] http://stev.oapd.inaf.it/cgi-bin/param_1.3

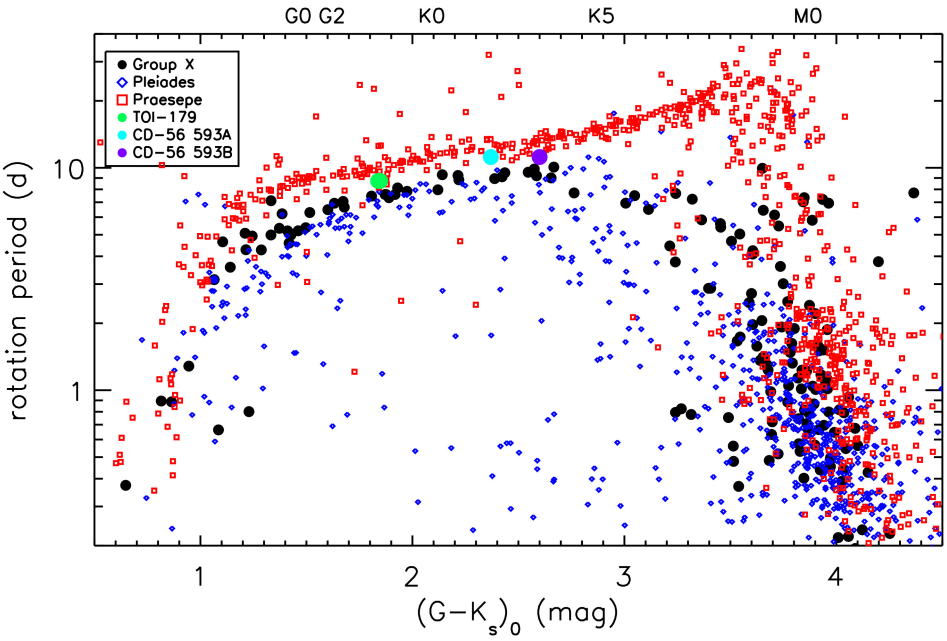

Fig. A.5: Rotation period of TOI-179 and CD-56 593A and B vs. $(G-K)_0$ color (green, cyan, and purple filled circles, respectively), compared to the members of the Pleiades and Praesepe open clusters (Rebull et al. 2016, 2017, plotted as blue diamonds and red squares, respectively) and Group X moving group (Messina et al. 2022, plotted as black circles). Only one photometric period is measured for CD-56 593, spatially unresolved in TESS images, and we are unable to determine to which component it belongs. The data are plotted in the figure for the colors of both components.

The stellar radius was derived through the Stefan–Boltzmann law, as was done in Carleo et al. (2021), using $T_{\rm eff}$ from Sect. A.1, V magnitude from Table 2, and bolometric correction from the Mamajek tables. The adopted radius is 0.767±0.024 $R_\odot$, slightly smaller but in agreement to better than 1σ with the results listed in the Gaia DR2, PIC, and TIC catalogs (Montalto et al. 2021; Stassun et al. 2019), and the EXOFOP database[16].

Coupling our adopted radius with the rotation period and projected rotational velocity from Sect. A.4 yields a stellar inclination of 90^{+0}_{-30} deg, with the expected equatorial velocity (4.44±0.15 km s^{-1}) nearly fidentical to the observed $v \sin i$ (4.5±0.5 km/s^{-1}). Therefore, the star appears to be seen close to edge-on. Alignment with the orbit of the transiting planets (i_b=87.5 deg, see Table 3) is then likely, although a moderate misalignment is possible within the error bars.

[16] https://exofop.ipac.caltech.edu/tess/target.php?id=207141131

Appendix B: Radial velocity and activity indicators time series

Table B.1: Radial velocities from TOI-179 HARPS spectra with uncertainties obtained from the TERRA pipeline. The corresponding measure of the bisector span is provided by the HARPS DRS. The Hα and the S-index with corresponding uncertainties are obtained with ACTIN.

6980.69590864	2.0808	0.9411	0.005250	0.2566	0.0004	0.3663	0.0021
6980.70195011	0.0000	0.8142	0.005890	0.2550	0.0004	0.3691	0.0028
6982.67878363	3.2470	1.1515	0.008210	0.2563	0.0005	0.3581	0.0027
6982.68488297	4.1855	1.2608	0.010610	0.2590	0.0006	0.3653	0.0025
6987.63091820	-29.3223	1.3290	0.055070	0.2593	0.0006	0.3553	0.0031
6987.63707540	-30.5069	1.4453	0.052730	0.2596	0.0006	0.3584	0.0021
6988.69275587	-32.0267	0.8648	0.044450	0.2581	0.0004	0.3511	0.0029
7223.88142723	-43.2483	2.0742	0.017150	0.2600	0.0007	0.3734	0.0021
7223.89251559	-38.0497	2.2566	0.019390	0.2604	0.0007	0.3426	0.0025
7224.88157860	-71.0729	1.7280	0.058330	0.2564	0.0006	0.3383	0.0026
7224.88963445	-69.1581	1.4157	0.056530	0.2561	0.0006	0.3367	0.0021
7333.76625907	-78.6104	0.9334	0.054490	0.2611	0.0003	0.3413	0.0019
7333.77693008	-78.3213	1.0476	0.060910	0.2601	0.0003	0.3473	0.0013
7342.74185760	-98.4356	1.1666	0.068750	0.2623	0.0003	0.3497	0.0014
7342.75252857	-96.7108	1.1087	0.067700	0.2625	0.0003	0.3411	0.0014
7344.69134515	-27.4767	1.0305	0.012730	0.2550	0.0003	0.3412	0.0013
7344.70191194	-28.9744	1.2010	0.011800	0.2559	0.0003	0.3364	0.0014
7600.82445252	-15.0062	2.7856	0.021910	0.2596	0.0008	0.3348	0.0014
7600.83648994	-17.2872	4.7693	0.009610	0.2605	0.0013	0.3269	0.0032
7713.80082617	-26.4906	1.5446	0.031270	0.2572	0.0004	0.3120	0.0046
7713.81152026	-25.8336	1.1222	0.035130	0.2573	0.0004	0.3580	0.0020
7770.61269041	0.4020	1.1772	0.021300	0.2674	0.0003	0.3512	0.0019
7770.62324557	2.3310	1.3228	0.020580	0.2658	0.0003	0.3763	0.0016
8007.71941096	-35.0594	1.9859	0.027950	0.2605	0.0007	0.3803	0.0018
8007.73070737	-37.9881	2.4466	0.023290	0.2614	0.0008	0.3356	0.0029
8035.62399563	-12.9255	1.1087	0.022640	0.2575	0.0004	0.3148	0.0034
8035.63478257	-13.3406	0.9869	0.019700	0.2580	0.0004	0.3460	0.0016
8039.62904707	-13.0419	1.1157	0.041150	0.2612	0.0004	0.3490	0.0015
8039.63992657	-12.7141	1.1839	0.042290	0.2615	0.0004	0.3660	0.0016
8417.56050911	15.8051	1.6301	0.039980	0.2675	0.0006	0.3637	0.0016
8417.76713698	1.5168	1.6723	0.030110	0.2685	0.0006	0.3968	0.0014
8418.55583647	-36.2440	1.3023	0.061410	0.2694	0.0005	0.3701	0.0020
8418.72027757	-40.3748	1.4555	0.074110	0.2648	0.0004	0.3801	0.0019
8419.68677382	-18.8122	1.2185	0.045670	0.2608	0.0004	0.3749	0.0017
8422.83131156	30.2399	2.3066	-0.020340	0.2626	0.0008	0.3815	0.0017
8423.74520254	-8.5072	1.4759	0.056360	0.2612	0.0005	0.3821	0.0016
8429.76226288	-12.5505	1.5425	0.048860	0.2593	0.0005	0.3872	0.0016
8430.74908821	2.3853	1.7303	0.026080	0.2664	0.0004	0.3682	0.0021
8431.67791694	26.4825	1.4431	-0.000970	0.2622	0.0004	0.3774	0.0013
8432.68523840	-24.2928	1.2659	0.081430	0.2608	0.0004	0.3943	0.0016
8432.71563107	-24.8233	1.3730	0.079500	0.2609	0.0005	0.3784	0.0020
8464.72530016	-9.8082	1.6310	-	0.2633	0.0006	0.3786	0.0013
8464.73352901	-6.8396	1.7945	-	0.2618	0.0006	0.3736	0.0017
8465.69725272	35.3156	1.5869	-	0.2711	0.0004	0.3797	0.0016
8465.70501861	33.8672	1.4372	-	0.2705	0.0004	0.3830	0.0016
8466.68945895	-26.6290	1.3620	-	0.2670	0.0005	0.3944	0.0018
8466.69655358	-26.1766	1.6262	-	0.2655	0.0005	0.3850	0.0021
8481.60390690	-0.1308	1.4002	-	0.2654	0.0005	0.3833	0.0018
8483.60647679	7.4831	1.1414	-	0.2719	0.0004	0.3808	0.0016
8509.53123346	-34.2170	1.6320	0.053220	0.2649	0.0005	0.3907	0.0016
8509.57920635	-34.3604	2.0194	0.064890	0.2689	0.0006	0.3865	0.0015
8509.59794413	-39.5850	1.8169	0.051320	0.2676	0.0006	0.3859	0.0023
8510.55122193	-42.5098	1.9474	0.057400	0.2596	0.0007	0.3943	0.0016
8510.58082740	-37.6804	2.6694	0.052610	0.2611	0.0007	0.3990	0.0014
8511.54866504	35.0932	1.5730	-0.008900	0.2636	0.0005	0.3919	0.0014
8511.60528350	38.0889	1.6384	-0.014010	0.2647	0.0006	0.3790	0.0017
8512.55084217	15.5591	1.4106	0.026710	0.2649	0.0004	0.3775	0.0017

Table B.1: continued.

BJD_{TDB} - 2450000	RV [m s^{-1}]	err_{RV} [m s^{-1}]	BIS [km s^{-1}]	Hα[1.6 Å] -	$err_{H\alpha[1.6Å]}$ -	S-index -	$err_{S-index}$ -
8576.48050990	0.4351	2.4353	0.044050	0.2760	0.0007	0.3766	0.0024
8576.51237350	-5.4469	3.4031	0.067490	0.2744	0.0012	0.3848	0.0025
8579.49225408	-44.4058	1.9851	0.085650	0.2655	0.0006	0.3899	0.0026
8580.47997019	14.8276	1.4775	0.020970	0.2663	0.0004	0.3918	0.0024
8581.48412227	5.2024	1.7351	0.032370	0.2634	0.0005	0.3973	0.0022
8582.47372628	34.2823	1.6718	0.007800	0.2689	0.0004	0.3890	0.0023
8670.93364852	6.9920	1.0773	0.046050	0.2717	0.0004	0.3866	0.0014
8673.87429327	31.5917	1.4553	-0.011120	0.2677	0.0006	0.3766	0.0019
8674.94274813	-9.4457	1.3615	0.049300	0.2690	0.0005	0.4005	0.0022
8684.87453781	17.8999	1.2278	0.013930	0.2660	0.0005	0.3750	0.0032
8689.86328901	2.8129	1.1143	0.041050	0.2684	0.0004	0.3819	0.0022
8690.87555738	39.9991	1.2297	-0.001130	0.2693	0.0005	0.3880	0.0039
8692.81900246	14.0329	1.0153	0.026230	0.2709	0.0004	0.4076	0.0019
8693.85287935	-2.9615	1.5832	0.045490	0.2672	0.0006	0.3861	0.0021
8694.84459014	0.2584	0.9592	0.024070	0.2686	0.0003	0.3842	0.0026
8695.87172996	50.5443	1.3158	-0.015140	0.2718	0.0004	0.3804	0.0017
8697.78683736	-35.8855	1.4054	0.077990	0.2667	0.0005	0.3793	0.0017
8698.82266843	8.1072	1.0585	0.025040	0.2646	0.0003	0.3624	0.0013
8699.88169423	37.6680	1.2428	-0.016730	0.2710	0.0005	0.3513	0.0034
8700.87854176	0.0000	1.1900	0.058290	0.2700	0.0004	0.3666	0.0019
8701.80598865	26.7346	1.3374	-0.000930	0.2690	0.0004	0.3542	0.0021
8702.76752183	-6.0488	1.2357	0.067500	0.2760	0.0005	0.3561	0.0018
8704.79732613	38.6818	1.4503	0.008390	0.2709	0.0005	0.3612	0.0016
8707.90966982	28.4307	1.3332	-0.002070	0.2666	0.0005	0.3600	0.0015
8708.76447295	40.6240	1.1993	0.002630	0.2675	0.0004	0.3577	0.0020
8718.74961073	36.4584	1.2453	0.001510	0.2756	0.0005	0.3602	0.0024
8719.82471466	-22.4962	1.1639	0.065630	0.2696	0.0004	0.3639	0.0026
8720.84621731	11.7789	1.6623	0.011170	0.2703	0.0006	0.3673	0.0020
8721.75426804	48.0785	1.0905	0.002300	0.2699	0.0004	0.3635	0.0019
8722.74122029	17.4124	1.2063	0.029480	0.2744	0.0004	0.3701	0.0021
8723.73967682	-27.3998	1.0954	0.069110	0.2709	0.0004	0.3720	0.0022
8724.82311116	3.5745	1.4927	0.030230	0.2679	0.0005	0.3718	0.0017
8725.70980525	26.9388	1.1838	0.007080	0.2662	0.0004	0.3782	0.0017
8734.72757798	27.6453	1.5650	0.011550	0.2669	0.0006	0.4008	0.0034
8736.83306483	2.5551	1.9949	0.038890	0.2699	0.0006	0.3901	0.0047
8737.80234571	11.0414	1.7889	0.034790	0.2792	0.0007	0.3674	0.0030
8738.72461165	48.5519	1.8637	-0.004540	0.2728	0.0006	0.3556	0.0025
8739.74132231	9.4424	1.3690	0.046930	0.2720	0.0006	0.3488	0.0026
8740.72127274	0.5538	1.5103	0.028690	0.2699	0.0006	0.3696	0.0027
8741.71402357	-8.6865	0.9042	0.064880	0.2677	0.0004	0.3569	0.0019
8742.71298907	82.1742	1.3040	0.016950	0.2716	0.0005	0.3589	0.0019
8744.86529394	12.8029	1.6896	0.010220	0.2738	0.0005	0.3616	0.0023
8745.68610835	-4.1308	2.2643	0.047710	0.2716	0.0008	0.3767	0.0024
8746.72905288	32.9618	1.5638	-0.011710	0.2759	0.0006	0.3596	0.0025
8747.64660273	23.5623	2.8275	0.009380	0.2780	0.0010	0.3663	0.0025
8748.66608518	-2.7872	1.3049	0.043140	0.2731	0.0005	0.3500	0.0018

Appendix C: Posteriors of the joint RV+TESS photometry fit

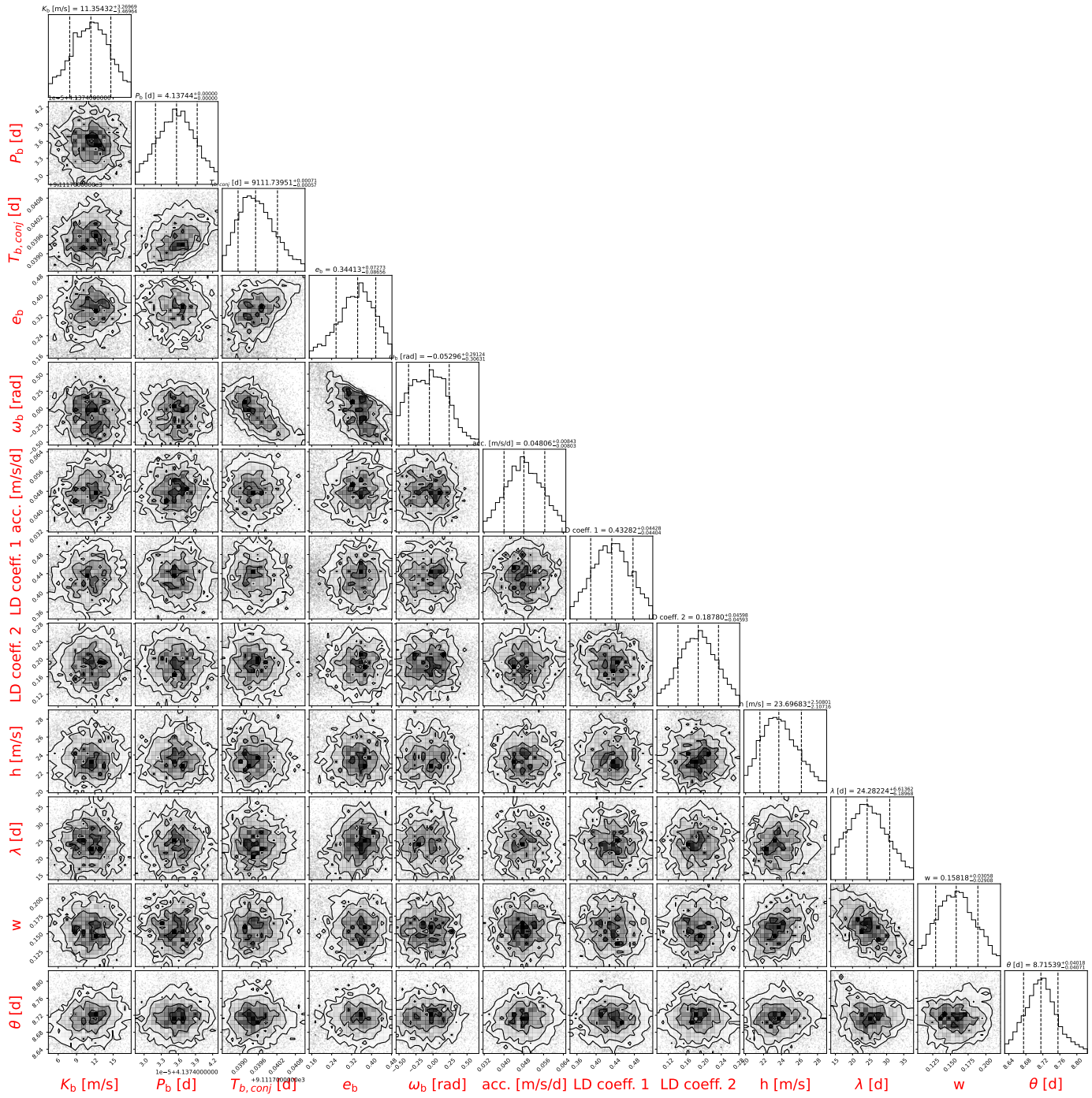

Fig. C.1: Posteriors of the free parameters used in the joint fit of the RV+TESS short-cadence light curve, including a linear long-term trend for the RVs (see Table 3). Two corner plots are shown for clarity.

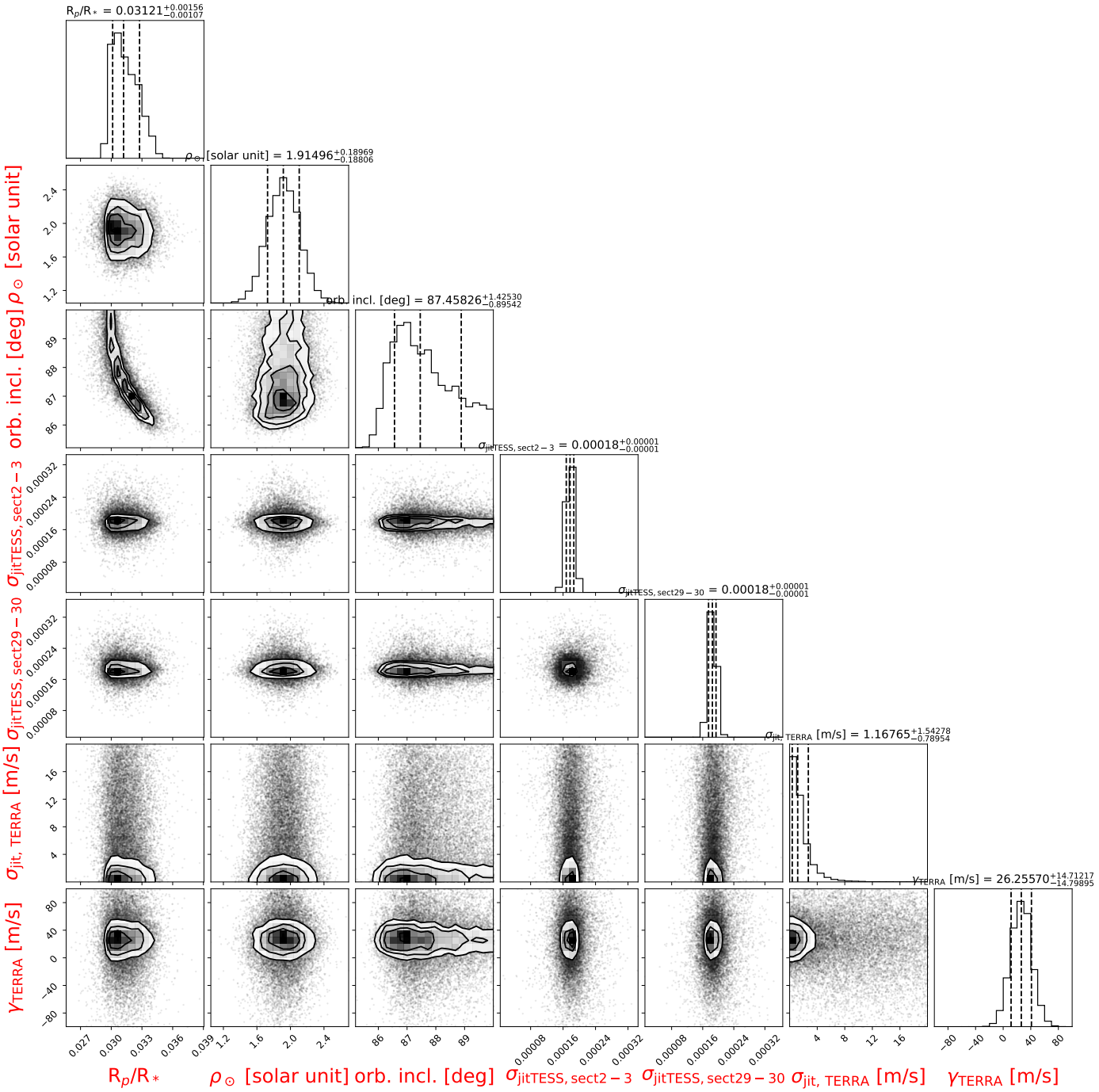

Fig. C.1: Continued